Type I interferon shapes the distribution and tropism of tick-borne flavivirus

Nunya Chotiwan[1,2,3*,#], Ebba Rosendal[1,2,#], Stefanie M. A. Willekens[1,2,4], Erin Schexnaydre[1,2,5,6], Emma Nilsson[1,2], Richard Lindqvist[1,2] , Max Hahn[4], Ionut Sebastian Mihai[2,7], Federico Morini[4], Jianguo Zhang[1,2,5,6], Gregory D. Ebel[8], Lars-Anders Carlson[2,5,6], Johan Henriksson[2,7] , Ulf Ahlgren[4], Daniel Marcellino[9], Anna K. Överby[1,2*]

[1] Department of Clinical Microbiology, Umeå University; 90185 Umeå, Sweden

[2] The Laboratory for Molecular Infection Medicine Sweden (MIMS), Umeå University; 90187 Umeå, Sweden

[3] Chakri Naruebodindra Medical Institute, Faculty of Medicine Ramathibodi Hospital, Mahidol University, Bangpla, Bangpli, Samutprakarn, 10540, Thailand

[4] Umeå Centre for Molecular Medicine (UCMM), Umeå University; 90187 Umeå, Sweden

[5] Wallenberg Centre for Molecular Medicine, Umeå University; 90187 Umeå, Sweden

[6] Department of Medical Biochemistry and Biophysics, Umeå University; 90187 Umeå, Sweden

[7] Department of Department of Molecular biology, Umeå University; 90187 Umeå, Sweden

[8] Department of Microbiology, Immunology and Pathology, Colorado State University, USA

[9] Department of Integrative Medical Biology, Umeå University; 90187 Umeå, Sweden

*Corresponding authors: Anna K Överby and Nunya Chotiwan

[#] Contributed equally

Email: anna.overby@umu.se and nunya.chotiwan@umu.se

Abstract

Several *Flaviviruses* are neurotropic and can cause encephalitis with significant long-term neurological sequelae. Viral tropism within the brain and the role(s) of vertebrate immunity in neurological disease is important to understand. We combined multimodal imaging (cm-nm scale) with single nuclei RNA-sequencing to study Langat virus in wildtype (WT) and IFN alpha/beta receptor knockout (*Ifnar*$^{-/-}$) mice to visualize viral pathogenesis and define molecular mechanisms. Whole brain viral infection was imaged by Optical Projection Tomography coregistered to *ex vivo* MRI. Infection was limited to gray matter of olfactory, visual and somatosensory systems in WT mice, but extended into white matter, meninges and choroid plexus in *Ifnar*$^{-/-}$ mice. All cell types in *Ifnar*$^{-/-}$ animals displayed strong proinflammatory and IFN-I-independent response, likely due to infiltration of *Ifng*-expressing CD8+NK cells, whereas in WT this was tightly controlled. Multimodal imaging-transcriptomics demonstrations that control of innate immunity is a critical factor in pathogenesis.

Introduction

Virus species from multiple families are able to cross the physical brain barriers, infect the central nervous system (CNS) and cause disease [1,2]. These include several neurotropic viruses from the genus *Flavivirus*, such as West Nile virus (WNV), Zika virus (ZIKV), Japanese encephalitis virus (JEV) and tick-borne encephalitis virus (TBEV). These flaviviruses frequently cause severe diseases in humans, including encephalitis and meningitis, and lead to significant mortality and long-term neurological sequelae among survivors [3-5]. While global disease burden remains high, no direct treatment for these viral infections is currently available. Consequently, patients rely solely on symptomatic treatment to moderate clinical disease and innate and acquired immune responses to respond to infection, ultimately resulting in virus clearance. Therefore, a better understanding of viral pathogenesis and the triggered immune response is required for the development of additional diagnostic tools, effective therapies, and preventive measures [6,7].

Induction of type I interferon (IFN-I) is a critical part of the host innate immune response, an important first-line defense against viral infection [8]. The IFN-I response can be activated locally in the CNS and is essential to protect the brain against neurotropic flaviviruses [9-11]. Furthermore, *in vitro* studies have demonstrated that the IFN-I response is rapidly induced in astrocytes upon TBEV infection and this response protects neurons from infection [12,13]. In models with a deficient or compromised IFN-I response, neurons and astrocytes were more susceptible *in vitro* [12,14]. In rodent models, this response limits the spread of viral CNS infection and protects mice from lethal encephalitis by Langat virus (LGTV), a less-virulent model for TBEV [9,15]. Furthermore, mice with a deficient IFN-I response showed increased inflammation, blood-brain barrier (BBB) breakdown and increased immune cell infiltration compared to wildtype (WT) mice after LGTV infection [9]. In addition to viral receptors and entry factors, the innate immune response is known to determine cell susceptibility to viral infection [14,16,17], yet how the IFN-I response influences this tropism and shapes global distribution of tick-borne flavivirus infection in the brain is not well understood.

Therefore, we infected WT mice and mice lacking the IFN-I response (*Ifnar*$^{-/-}$) intracranially with LGTV, monitored virus distribution in the brain using advanced imaging techniques and measured cellular responses to infection by single nuclei RNA sequence (snRNAseq). For a holistic view of viral brain infection, we devised an imaging approach that combines viral distribution in the whole brain (~0.5 cm^3), obtained by Optical Projection Tomography (OPT) [18], with detailed anatomic information provided by an *ex vivo* magnetic resonance imaging (MRI)-based brain template. We found gray matter (GM) of olfactory, visual and somatosensory areas infected in WT mice and this distribution expanded to white matter (WM) in the absence of IFN-I response. Using additional imaging modalities, extending down to nm scale, we found that the IFN-I response restricts viral replication in meninges and epithelial cells of choroid plexus (ChP). Interestingly, the cellular tropism of LGTV in cerebrum shifted from neurons in WT towards Iba1-positive cells in *Ifnar*$^{-/-}$ mice. We then used snRNAseq of cerebral cortex to clarify the transcriptional changes in different cell populations to identify the molecular mechanism of viral pathogenesis. We found that, without IFN-I signaling, the inflammatory response was skewed towards type II IFN (IFN-II) response, and observed infiltration of several distinct immune cell populations, including a large population of peripheral macrophages (MØs). Together, our data provide an unprecedented view of virus distribution and tropism within the brain and highlight the importance of local IFN-I induction and control in influencing virus distribution, tropism and pathogenesis.

Results

Whole brain 3D imaging and coregistration of LGTV infection with MRI in WT and Ifnar$^{-/-}$ *mice*

Local IFN-I restricts neurotropic flavivirus infection in rodent brain as demonstrated by nucleic acid amplification and immunohistochemistry assays [9,12,15,19]. However, these techniques do not provide a comprehensive understanding of viral distribution. Therefore, we set out to establish an imaging approach for neurotropic virus infection in whole mouse brain using OPT to specifically investigate the effect of IFN-I on viral distribution. To surpass brain barriers, we infected mice intracranially, and brains were collected at humane endpoint, 6-7 days and 4-5 days post-infection for WT and *Ifnar*$^{-/-}$, respectively (Supplementary

Fig. 1a). Whole brains were bleached to reduce auto-fluorescence, immunolabeled against LGTV nonstructural protein 5 (NS5), mounted in agarose, optically cleared, and scanned using OPT (Fig. 1a,b). Tomographic reconstruction enabled visualization of viral infection throughout the entire brain in 3D. Applying this method, we observed that viral infection in WT brains was predominantly localized in cerebral cortex, with weak signals in the olfactory bulb and with no detectable infection in lateral ventricles nor the fourth ventricle (Fig. 1c ii, Supplementary Fig.1b, and Supplementary Movie 1). In contrast, in *Ifnar*$^{-/-}$ brains, we observed weak infection throughout the cerebral cortex but a pronounced infection in the meninges, third ventricle, fourth ventricle, and the interior wall of the lateral ventricles, spanning into the anterior cerebrum and olfactory bulbs, a pattern closely resembling the rostral migratory stream (Fig. 1c iii, Supplementary Fig. 1 and Supplementary Movie 1). We also detected some low-level unspecific signal in uninfected brains (mock group) (Fig. 1c i and Supplementary Fig. 1b), indicating possible ventricular antibody trapping or a low, unspecific antibody absorption in meninges during whole brain immunolabeling.

Although OPT enables visualization of LGTV distribution in the whole brain with great sensitivity and high spatial resolution (Fig. 1c), the anatomical information obtained from tissue autofluorescence using this technique is insufficient to provide detailed anatomical information, especially in the cerebrum. As the brain is divided into multiple structures [20], linked to different physiological functions, it would be of great value to improve the anatomical reference frame, to allow a precise identification of infected brain areas. To address this, we acquired structural *ex vivo* MR images from brains after chemical preprocessing and OPT acquisition. These images were coregistered with viral OPT signal, which resulted in fusion images with good spatial alignment (Fig. 1d). In some infected brains, we also observed hyperintense lesions on the T1-weighted images, suggesting virus-induced damages (Fig. 1d i). To obtain a reference frame with improved anatomical detail and tissue contrast and to overcome high MRI-scanning costs of individual brains in the future, we created a high-resolution Optically Cleared UMeå (OCUM) brain template, which was generated from MR images acquired after tissue bleaching and clearing for optical imaging[21]. In optimized OPT-OCUM fusion images, viral signal is displayed within a detailed anatomical context, in 3D,

where neuronal pathways and trajectories can be observed, *e.g.*, the rostral migratory stream in an *Ifnar*$^{-/-}$ infected brain (Fig. 1e).

IFN-I response protects meninges and ChP from viral infection

In WT brains, we observed weak viral signal in the meninges and the interior wall of third ventricle on OPT (Fig. 2 and Supplementary Fig. 1b). However, we did not detect viral antigen in these regions by confocal microscopy (Fig. 2c and Supplementary Fig. 2), indicating non-specific antibody trapping in WT mice. In *Ifnar*$^{-/-}$ brains, on the other hand, we observed intense viral OPT signal within meninges, which was confirmed by confocal microscopy (Supplementary Fig. 2). Additionally, we observed strong viral signal located in all ventricles (Fig. 1c, 2a). To complement OPT data, we used light sheet fluorescence microscopy (LSFM) to obtain higher resolution images of viral signal in the fourth ventricle and found that ChP, the secretory tissue that resides within ventricles, was highly infected (Fig. 2b and Supplementary Movie 2). Confocal analysis confirmed that ChP of all ventricles, as well as the ependymal cells lining the ventricular walls, were highly infected in *Ifnar*$^{-/-}$ brains, but not in WT (Fig. 2c). To further evaluate cellular tropism within ChP, we stained *Ifnar*$^{-/-}$ brains with different cellular markers and the viral antigen (NS5) and found that viral infection colocalized with the epithelial cell marker aquaporin-1 (AQPI) in ChP (Fig. 2d). This finding is different from what was recently shown in ZIKV infected mouse brains, where ZIKV specifically targeted pericytes [22].

To further investigate the subcellular localization of virus particles within ChP epithelial cells, we imaged fourth ventricle ChP of *Ifnar*$^{-/-}$brain using electron microscopy. Transmission electron microscopy (TEM) of ChP epithelial cells, identified by the presence of cilia, revealed an extreme distortion of endoplasmic reticulum (ER) membranes in infected tissue as compared to mock infected brains (Fig. 2e), in line with previous findings for other flaviviruses in cell culture [23-26]. Higher resolution imaging revealed virus particles in the ER lumen (Fig. 2f, inset *i*) and formation of viral replication complexes as bud-like invaginations of the ER membrane (Fig. 2f, inset *ii*). Segmentation of volumetric images, taken by focused ion beam milling-scanning electron microscopy (FIB-SEM), depict the 3D architecture of replication complexes (Fig. 2g,h).

Replication vesicles were clustered together within a dilated ER, and virions were detected both within the infected cell and between two cells (visualized by green and blue; Fig. 2i), indicating active viral replication and viral spread within the tissue. TEM and FIB-SEM support earlier observations, confirming productive infection of epithelial cells of ChP in *Ifnar*$^{-/-}$ brains and provide insight into cytoarchitectural changes induced by viral infection *in vivo*. Taken together, the observed differences between WT and *Ifnar*$^{-/-}$ mice indicate that the IFN-I response efficiently restricts viral replication in the meninges, ventricles and ChP.

Neuronal circuit mapping and shift in cellular tropism of viral infection in cerebrum

Whole brain OPT-MRI enabled us to visualize and map viral distribution in the cerebral cortex to distinct areas (Fig. 3). In WT mice, viral signal was detected in entorhinal cortex, piriform area, primary visual field, and primary somatosensory cortex (upper limb), which are parts of the olfactory, visual, and somatosensory systems. These regions reside in GM (Fig. 3a, left panels), which consists of neuronal cell bodies. In contrast, *Ifnar*$^{-/-}$ mice displayed a more widespread distribution of viral infection, including GM, WM and the ventricular system (Fig. 3a, right panels). In GM, we observed viral signal within the granular cell layer of the olfactory bulb, entorhinal cortex, dorsal endopiriform nucleus, piriform area, agranular insula, primary visual field, and primary somatosensory cortex (upper limb and barrel field). In WM, we detected viral signal within the olfactory limb of the anterior commissure, anterior forceps of corpus callosum, and supra-callosal WM. These WM infected regions are also part of the olfactory, visual, and somatosensory systems. Of note, the lateral ventricle, subventricular zone, and the olfactory limb of the anterior commissure are all parts of the rostral migratory stream, which suggests specific LGTV infection of the ventriculo–olfactory neurogenic system in *Ifnar*$^{-/-}$ brains.

Cellular tropism in these infected brain regions were further investigated by confocal microscopy. In sections containing areas of rostral migratory stream, we observed viral infection in immature neurons, identified by doublecortin (DCX) immunoreactivity in both WT and *Ifnar*$^{-/-}$ brains (Fig. 3b). This indicates that immature neurons are susceptible to viral infection irrespective of type I IFN signaling of the host. On the other hand, no infection was found in astrocytes of either genotype (Fig. 3c). This is in contrast to

147 primary astrocytes in cell culture, which were found to be highly infected by several neurotropic flaviviruses
148 in the absence of IFNAR [12]. Focusing on the cerebrum, the majority of infected cells in WT brains were
149 neurons, which have round-cell body morphology and reside in GM, whereas only 10.5 ± 3.61% of all
150 infected cells in cerebrum were positive for the microglial marker Iba1 (Fig. 3d-f). In *Ifnar*$^{-/-}$ brains,
151 surprisingly, we observed a shift in cellular tropism from neurons to microglia in which half (50.5 ± 9.87%)
152 of infected cells were Iba1-positive (Fig. 3d-f). To further investigate this phenomenon in another system,
153 we isolated primary microglia from neonatal WT and *Ifnar*$^{-/-}$ brains and infected them *in vitro*. Independently
154 of IFNAR protein expression, microglia exhibited low susceptibility to LGTV infection *in vitro* (Supplementary
155 Fig. 3).
156
157 Taken together, while viral infection is restricted predominantly to neuronal cell bodies of olfactory, visual
158 and somatosensory systems of GM in WT, viral tropism expands to WM in the absence of IFN-I signaling.
159 *In vivo,* cellular tropism was also found to shift towards Iba1-positive cells in the absence of IFN-I signaling,
160 however this tropism shift is not observed in primary microglia from *Ifnar*$^{-/-}$ mice *in vitro*.
161
162 **Single nuclei RNA sequencing analysis of virus-induced cellular responses**
163 The increased susceptibility of *Ifnar*$^{-/-}$ Iba1-positive microglia *in vivo* compared to primary microglia *in vitro,*
164 indicates that additional factors of the cellular milieu in the brain influence the tropism of LGTV infection in
165 the absence of IFN-I signaling. Alternatively, this shift in tropism might be a result of Iba1 expressing
166 infiltrating MØ that have been detected in the brain after LGTV infection [9]. To investigate these hypotheses,
167 we performed droplet-based single nuclei transcriptomic analysis (10x) of cerebral cortex isolated from
168 LGTV infected WT and *Ifnar*$^{-/-}$ mice as well as for uninfected controls (Fig. 4a). After data processing and
169 quality control, we obtained a total of 28,298 nuclei with a median of 1,260 genes detected per nucleus.
170 Using graph-based clustering and analysis of established marker genes, we identified cells of each major
171 cell type expected in cerebral cortex; *i.e.*, neurons, astrocytes, microglia, oligodendrocytes, oligo progenitor
172 cells (OPCs), endothelial cells, vascular leptomeningeal cells (VLMCs) and pericytes (Fig. 4b-d,
173 Supplementary Table 1). We also detected a small population of *Ttr* expressing cells, most likely

174 representing residual ChP epithelial cells [27]. Interestingly, we also identified cells corresponding to CD8+NK
175 cells in infected *Ifnar*$^{-/-}$ brains, but not in WT or uninfected controls.
176
177 To understand the fundamental differences between WT and *Ifnar*$^{-/-}$ mice, we first analyzed differential
178 gene expression in all cell types from uninfected animals. Although we previously reported that primary
179 astrocytes from WT and *Ifnar*$^{-/-}$ mice, cultured *in vitro,* display major expression differences at baseline [12],
180 our snRNAseq analysis of all cell types presented very little differences *in vivo* (Supplementary Fig. 4a).
181 Subsequently, we evaluated the differentially expressed genes (DEGs), in response to LGTV infection for
182 each cell type of WT and *Ifnar*$^{-/-}$ brains, and performed gene set enrichment analysis (GSEA) on
183 REACTOME pathways. Surprisingly, in WT brain we identified only a limited number of DEGs (640), with
184 the majority of expression changes in microglia, astrocytes and oligodendrocytes (Fig. 4e, Supplementary
185 Table 2). Although we detected a similar viral load in cerebral cortex of WT and *Ifnar*$^{-/-}$ mice at endpoint
186 (Supplementary Fig. 4b), the response to viral infection in *Ifnar*$^{-/-}$ was notably stronger in all cell types, with
187 a greater number of identified DEGs (2,952) compared to WT (Fig. 4e, Supplementary Table 2). The
188 majority of DEGs for both WT and *Ifnar*$^{-/-}$ were found to be upregulated (Supplementary Table 2). We
189 compared the overlap of upregulated DEGs amongst the five most responsive cell types based upon
190 number of DEGs (astro, micro/MØ, oligo, VLMCs and endo) (Fig. 4f). In WT mice, only five genes,
191 corresponding to 1.9% of all upregulated DEGs, were commonly upregulated in these cells (Supplementary
192 Fig. 4c), indicating that majority of responses are unique to each cell type. While for *Ifnar*$^{-/-}$ this was
193 increased to 95 genes, corresponding to 12% of all upregulated DEGs, showing a greater overlap and
194 uniform cell response to infection. Among the shared genes upregulated for both genotypes, we identified
195 cytokines such as *Ccl5* and *Cxcl10,* as well as genes related to neuroinflammation, such as *Apod, Mt1* and
196 *Mt2*. In brains of infected *Ifnar*$^{-/-}$ mice, we also observed a broad upregulation of additional proinflammatory
197 cytokines (*Ccl2, Ccl4),* IFN stimulated genes *(Rsad2, Mx1, Isg15*, *Ifit1-3)* and genes encoding MHC class I
198 proteins (*H2-D1, H2-K1*). In accordance with these observations, we found a greater number of significant
199 pathways in *Ifnar*$^{-/-}$ compared to WT (Fig. 4g, Supplementary Table 3).
200

Unexpectedly, in WT mice, the IFN signaling pathway was induced in only a few cell types, including astrocytes and VLMCs (Fig. 4h) while it was the most upregulated pathway in all cell types for *Ifnar*$^{-/-}$. This indicates an IFN-I independent upregulation of these genes or that other IFNs, *e.g.*, IFN-II or IFN-III, compensate for the absence of IFN-I signaling. Therefore, we specifically evaluated expression changes of IFN-II (*Ifng*) and IFN-III (*Ifnl1-3*). Although we could not find expression of IFN-III in any cell type, we found that particularly CD8+NK cells strongly expressed *Ifng* in *Ifnar*$^{-/-}$ (Fig. 4i). IFNγ is known to compensate for lack of IFN-I and can exert non-cytolytic antiviral activity against WNV, Sindbis virus and measles virus infection in neurons [28-31]. It can also act as proinflammatory and exaggerate pathogenesis by upregulating MHC class I expression and antigen presentation [32,33]. We found that all cell types of *Ifnar*$^{-/-}$ mice upregulate the antigen processing and cross-presentation pathway (Fig. 4h). Several genes encoding proteins that make up the MHC class Ia and Ib showed elevated expression levels in all cell types in infected *Ifnar*$^{-/-}$ mice but were only modestly upregulated in endothelial cells of infected WT mice (Supplementary Fig. 4d).

Since *Ifng* expressing CD8+NK cells might contribute to increased inflammation in infected *Ifnar*$^{-/-}$ mice, we evaluated the expression of known T-cell chemoattractants (Supplementary Fig. 4e) and observed an increase in *Ccl2, Ccl5 and Cxcl10* levels in infected *Ifnar*$^{-/-}$ compared to WT mice. Furthermore, VLMCs, pericytes and endothelial cells of *Ifnar*$^{-/-}$ mice expressed high levels of *Cxcl9,* a chemokine dependent on IFNγ for cerebral expression [34]. This further confirms the role of IFN-II signaling in the brain of these mice. A high expression of corresponding receptors *Ccr2* and *Ccr5* were found in micro/MØ and CD8+NK cells (Supplementary Fig. 4e). We performed subclustering of the infiltrating CD8+NK cell population but were unable to obtain a clear separation between CD8+ and NK cells. These cells express both NK cell (*Klrblc, Klrd1, Nrc1* and *Nkg7*) and CD8+ T-cell associated genes (*Cd3g, Cd3d, Cd28, Cd8a* and *Cd8b1*) (Fig. 5a). Both CD8+ and NK cells use granzyme A (*Gzma*), granzyme B (*Gzma*) and perforin (*Prf1*) to kill target cells [35] which may contribute to immunopathology. These genes were all found to be upregulated in our dataset (Fig. 5b), indicating that these infiltrating cytotoxic cells may contribute to tissue disruption. We also investigated whether any infiltrating CD8+ or NK cells in *Ifnar*$^{-/-}$ were infected using confocal microscopy

(Supplementary Fig. 5a,b). We were unable to detect virus-positive CD8+ cells, nor infected CD335 positive cells, indicating that these infiltrating cells are not a major viral target in *Ifnar*$^{-/-}$ mice.

As we detected a shift in viral tropism towards Iba1-positive cells in *Ifnar*$^{-/-}$ mice (Fig. 3e,f), it is interesting that the total number of microglia/MØ increased upon infection (from 3.7% to 26%) in contrast to that of WT, which remained at low levels (4.2% vs. 3.6%) (Fig. 4c). This suggests infection of proliferating resident microglia and/or infiltrating peripheral MØs. By a subclustering of the microglia/MØ population, we identified in addition to microglia (*Cxcr1*) and MØ (*Slfn4*), a cluster of monocyte-like cells (*Ccl3*, *Ccl4, Il12b* and *Tnf)* and a small number of neutrophils (*S100a9*, *S100a8* and *Clec4d*) in *Ifnar*$^{-/-}$ mice (Fig. 5c). In WT mice, we found predominantly microglia regardless of infection (Fig. 5d, left panel), while in *Ifnar*$^{-/-}$, we observed a shift in cell proportions from microglia in uninfected mice towards a majority of MØ during infection (Fig. 5d), which is in line with previous reports for Rabies virus [36]. Since we were unable to separate infected versus uninfected cells with this snRNAseq dataset, we used immunohistochemistry to determine the cellular identity of cells infected in *Ifnar*$^{-/-}$ mice. Brain sections triple-immunolabelled for viral antigen, Iba1 and the microglia specific marker TMEM119 [37] (Fig. 5e). In WT mice, multiple activation states of uninfected microglia were identified by microglial morphology (Fig. 5f). In *Ifnar*$^{-/-}$ mice, the majority of LGTV infected cells were positive for TMEM119 (Fig. 5f) further demonstrating the shift in cellular tropism in the absence of IFN-I signaling. However, Iba1-positive TMEM119-negative infected cells were occasionally detected (Fig. 5f). Together, this strongly suggests that the majority of infected cells in *Ifnar*$^{-/-}$ are not infiltrating MØs but of microglial origin, probably rendered susceptible by the local inflammatory milieu *in vivo*.

Discussion

While it is clear that the IFN-I response limits viral replication in the brain, viral distribution and cellular tropism on a global whole-brain level have not been addressed. In this study, using multiple imaging modalities (ranging from cm to nm resolution), we evaluated the impact of the IFN-I response on viral distribution within the whole brain with high resolution MRI-guided anatomical precision. We show that type I IFN response specifically limits LGTV replication in ChP and cerebral WM. We also show that the specific

255 interplay between cells and the local milieu *in vivo*, determine the susceptibility to viral infection. In the
256 absence of IFN-I response, uncontrolled inflammation is induced which is skewed towards an IFN-II
257 response and a cellular tropism shift to microglia.
258
259 To date, the details regarding viral brain infection and pathogenesis have been partially concealed by an
260 inability to visualize viral infection on the whole organ level. OPT and LSFM are 3D imaging techniques for
261 transparent mesoscopic-sized (mm-cm) tissue samples; and are therefore suitable for rodent whole brain
262 imaging. These methods provide information at cellular resolution while still capturing the entire tissue in
263 3D and have been used in various applications for targeted imaging [38-40]. However, anatomical information
264 obtained from OPT, based on tissue autofluorescence, is limited. MRI, conversely, is widely used for
265 anatomical brain imaging since it has exquisite contrast and resolution [41]. Structural MRI is not suitable for
266 imaging pathogens, but when combined with OPT, one could gain information on both viral distribution and
267 its anatomical location. Several mouse brain templates are available. However, they are either based on
268 histology [20,42] or, *in vivo* or *ex vivo* MRI *in situ* [43-45]. OPT imaging of whole brain viral signal is acquired *ex*
269 *vivo* after tissue bleaching and optical clearing. These chemical treatments result in a certain degree of
270 tissue shrinkage, which leads to misalignment when coregistering brain OPT signals to existing templates.
271 Therefore, we used the OCUM brain template[21], specifically designed and created from *ex vivo* MR images
272 after OPT pre-processing, yielding improved alignment and precise anatomical mapping of virus distribution
273 in the brain.
274
275 Here, we studied the effect of the local IFN-I response on LGTV neurovirulence in the brain after intracranial
276 infection. This model was chosen to eliminate all peripheral IFN effects and to provide the virus full access
277 to the brain. OPT-MRI fusion images, together with LSFM, revealed widespread viral infection in olfactory
278 bulb, rostral migratory stream, ventricles, ChP, GM and WM, and showed that whole brain infection patterns
279 are influenced by the IFN-I response. Interestingly, at endpoint, meninges and ChP were only infected in
280 *Ifnar*$^{-/-}$ brains. This is similar to Herpes Simplex virus I (HSV1) and ZIKV, where viral infection is detected
281 in ChP of *Ifnar*$^{-/-}$ brains but not in WT mice [22,46]. This strongly suggests that the IFN-I response plays a

major role in preventing viral infection in ChP. Of note, while we detected productive LGTV infection in ChP epithelial cells, a previous study found that ZIKV mainly infects pericytes in ChP [22], indicating tropism differences exist among neurotropic flaviviruses. In cerebrum, infection in both WT and *Ifnar*$^{-/-}$ was predominantly restricted to regions processing olfactory, visual and somatosensory information. These regions have previously been reported in animal experiments of other neurotropic flaviviruses, such as TBEV and JEV [47,48]. The olfactory system was most infected and widespread in *Ifnar*$^{-/-}$ compared to WT, with virus signal in areas processing sensory input from the olfactory bulb (granular cell layer of olfactory bulb) and areas involved in processing and integrating olfactory and gustatory information (piriform cortex, endopiriform nucleus and agranular insula, all located in the orbitofrontal cortex). Furthermore, endopiriform nucleus consists of specialized cells with long axons projecting towards, among others, the entorhinal cortex, located at the caudal end of the temporal lobe, another cortical area identified to be infected in our study. While anosmia (loss of smell) is not a common symptom in tick-borne encephalitis patients, nor has it been tested in animal models, a case with anosmia post TBEV vaccination has been reported [49]. Other flaviviruses such as ZIKV, WNV, and JEV were described to target regions of hippocampus and affect learning and memory [50-52]. We however did not see specific targeting of hippocampus by LGTV in WT nor *Ifnar*$^{-/-}$ mice by whole brain imaging. Although hippocampus was not infected by LGTV in WT mice, similar to reports by others, LGTV in WT mice caused impaired memory function and anxiety–like behaviors [53]. Interestingly, we observed hyperintense lesions on T1-weighted images of infected brains, which is in line with imaging data obtained from TBE patients, which predominantly show lesions in the basal ganglia, thalami and cerebellum [54]. Interestingly, post-mortem IHC of TBEV brains showed the presence of virus in these regions [55]. However, in our study, the cortical lesions detected on T1 images appeared to be much more widespread than the viral signal detected by OPT. These observations suggest that CNS damage cannot be explained only by the presence of virus in a particular area and suggest neuroinflammation-induced lesions.

Single cell or snRNAseq is a useful tool to study the transcriptional response in specific cell types upon infection or inflammation. In contrast to bulk RNA sequencing or microarray analysis of tissue [56,57], where

the combined response of all cells is measured, we show that in WT mice, the response to infection was highly cell-type specific and that the identified upregulated pathways showed a balance between pro- and anti-inflammatory signaling. While scRNA sequencing of Rabies virus infected WT mice showed a very strong pro-inflammatory response [58], we detected a relatively low number of DEGs after LGTV infection in WT mice. In contrast to Rabies virus, where IFNβ was detected in microglia [58], we found a broader expression of IFNβ, but only astrocytes and VLMCs showed an IFN-I-like response after LGTV infection. This is in sharp contrast to mouse hepatitis virus where a strong antiviral response is elicited in the brain [57]. This discrepancy might be due to the time point post infection of the analysis as it has been shown that the IFN-I response within the brain is transient and dampened with time by the expression of negative regulators to limit cytotoxic effects [59]. Even though we detected a similar viral load in cerebral cortex of WT and *Ifnar*$^{-/-}$ mice, the transcriptional profiles were markedly different, and a large number of DEGs were upregulated independently of IFNAR signaling. This IFN-I-independent immune response has also been observed for vesicular stomatitis virus (VSV) [56]. In this case, IFNγ in combination with TNFα and IRF1 compensate for the loss of IFN-I response [56]. We observed a large overlap between cell types among the upregulated genes in *Ifnar*$^{-/-}$ mice, and these were mainly related to IFN signaling and antigen presentation. Similar to VSV, we found IRF1 to be upregulated in all cell types and TNFα was expressed in monocyte-like cells as possible compensation for lack of IFNAR. Although, a strong antiviral response was elicited in all cell types upon the infection of *Ifnar*$^{-/-}$mouse brain, it might be that the IFNγ antiviral response is not optimal, due to the lack of communication between IFNα/β and IFNγ signaling pathways [60]. It has also been shown that IFN-I response may negatively regulate IFN-II-dependent immune cell infiltration into the CNS (reviewed in: [61]), and in its absence, the infiltrating immune cells cause pathology. Concordantly, we observed CNS infiltration of several immune cell populations such as CD8+NK cells, MØs, neutrophils and atypical monocytes in *Ifnar*$^{-/-}$, but not in WT mice. This exaggerated immune infiltration may contribute to reduced lifespan of *Ifnar*$^{-/-}$ after LGTV infection. Others have shown that mice depleted in CD8+ T-cells show prolonged survival following TBEV infection [62]. The role of CD8+ T-cells has also been thoroughly studied for mosquito-borne flaviviruses, especially WNV, where they play a dual role, both contributing to viral clearance and immunopathology within the CNS [63-66]. Accordingly, the CD8+ cell population detected

in *Ifnar*$^{-/-}$ after LGTV infection may contribute to the pro-inflammatory state, via IFNγ expression, the pathology, and the rapid disease course.

We observed infection in both WM and GM in *Ifnar*$^{-/-}$ brains, while infection in WT brains was mostly restricted to the latter. This restriction to GM might relate to the surprising shift in cellular tropism from neurons in WT to Iba1-positive cells in *Ifnar*$^{-/-}$ mice. Interestingly, we did not detect Iba1-positive infected cells in cerebellum nor the brain stem in *Ifnar*$^{-/-}$ mice, indicating location specific differences of Iba1-positive cell populations. The observed tropism shift and increase in Iba1-positive cellular infection by LGTV in cortex is similar to what was observed in STING-deficient mice, infected with HSV-I [67]. Interestingly, we observed an increase in proportion of microglia/MØ in the cortex of *Ifnar*$^{-/-}$ mice upon infection using snRNAseq. Sub-clustering of these cells showed a dominance of what is likely infiltrating MØ. However, the majority of the infected Iba1-positive cells were TMEM119 positive, indicating that resident microglia and not MØ are targeted by virus. We can only speculate why this infected population of microglia was undetected in the snRNAseq, but it has been reported that infected cells become fragile during processing of single cell RNA sequencing [36]. Proper activation of microglia in olfactory bulb requires IFNAR signaling in neurons and astrocytes but not in microglia [68]. Interestingly, we observed that cortical TMEM119 immunoreactivity was stronger in infected WT mice compared to infected *Ifnar*$^{-/-}$ (Fig. 5f) indicating that a similar mechanism of microglial activation might occur in cortex. In line with this, infection of cultured primary microglia from cortex showed low susceptibility to LGTV infection, independent of IFNAR expression. This discrepancy between *in vitro* and *in vivo* experimentation strongly indicates that cellular communication between neurons, astrocytes and microglia, which produce a local milieu within the brain, dictates the outcome and susceptibility of infection. Therefore, one should be cautious when extrapolating *in vitro* findings to the *in vivo* setting.

Here, we investigated the effect of the local IFN-I response on tick-borne flavivirus neurotropism. Using multimodal imaging, spanning a range from cm to nm, we were able to anatomically map viral distribution and identify target cells where we could visualize active replication and the release of virions. We found

that the IFN-I response shapes viral distribution in various neuronal pathways and brain regions as well as its cellular tropism. Together, these results suggest that cell types or cell populations that belong to different brain areas may respond to viral infection in different ways, and that the response is highly region- and cell-specific. Additionally, we used snRNAseq to analyze the cellular response following infection and define the molecular mechanisms of pathogenesis. We found that IFN-I signaling primarily balances the natural inflammatory response, as very few antiviral genes were upregulated in the brain. In its absence, uncontrolled proinflammatory responses were elicited with *Ifng* expression and infiltration of MØ, CD8+ and NK cells. We also show that this proinflammatory milieu within the brain most likely shifts viral tropism to resident microglia which become the main target of infection. Collectively, our approach provides unprecedented insight into the outcome of viral infection, the importance of IFNs and the molecular mechanism of viral pathogenesis. Future studies are still required to systematically explore the temporal, spatial and cellular responses to viral infection to understand the effects of the IFN response in full, and to improve our understanding of viral neuropathogenesis.

Methods

Animals

C57BL/6 WT mice and *Ifnar*$^{-/-}$ mice in C57BL/6 background were kindly provided by N.O. Gekara [8] Mice were bred as homozygotes and maintained under specific pathogen-free conditions Animal experiments were approved by the regional Animal Research Ethics Committee of Northern Norrland and by the Swedish Board of Agriculture (ethical permits: A9-2018 and A41-2019), and all procedures were performed according to their guidelines.

Viruses

LGTV strain TP21 was a kind gift from G. Dobler. LGTV stock was produced in VeroB4 cells, a kind gift from G. Dobler [26] and harvested on day 3 post infection when cytopathic effects were apparent. Virus

389 supernatant was harvested on day 7 post-infection and titrated on VeroB4 cells using focus-forming assay
390 [26].
391
392 ***Virus infection model in the mouse***
393 Animals (7- to 13-week-old, mixed gender) were either left untreated, mock-treated (PBS) or infected with
394 LGTV. After sedation with ketamine (100 µg/g body weight) and xylazine (5 µg/g body weight) or Isoflurane,
395 animals were intracranially inoculated with indicated dose of LGTV suspended in 20 µL PBS. Infected mice
396 were euthanized using oxygen deprivation when they developed one severe symptom, such as: >20%
397 weight loss, bilateral eye infection, diarrhea or hind-limb paralysis; or when they developed three milder
398 symptoms, such as: >15% weight loss, unilateral eye infection, facial edema, ruffled fur or overt
399 bradykinesia, and/or development of stereotypies.
400
401 ***Whole-mount immunohistochemistry (IHC) and OPT***
402 Following euthanasia, cardiac perfusion was performed using 20 mL PBS followed by 20 mL 4% w/v
403 paraformaldehyde (PFA) in PBS, after perfusion, brain was removed and further immersed in PFA for 2 h
404 before thoroughly washed by PBS. PFA-fixed brains were fluorescently immunolabeled with an antibody
405 against viral NS5 and processed for OPT imaging, as previously described [38,69]. Briefly, the brain was
406 dehydrated in a stepwise gradient of methanol (MeOH), permeabilized by repeated freeze–thawing in
407 MeOH at –80 °C and bleached in a solution (MeOH:H_2O_2:DMSO at 2:3:1) to quench tissue
408 autofluorescence. Specimen were rehydrated in TBST (50 mM Tris-HCl, pH 7.4, 150 mM NaCl, and 0.1%
409 v/v TritonX-100), blocked with 10% v/v normal goat serum (NGS) (#CL1200-100, Nordic Biosite, Sweden),
410 5% v/v DMSO, and 0.01% w/v sodium azide in TBST at 37 °C for 48 h, and labeled with primary (chicken
411 anti-NS5; Supplementary Table 4)) and secondary (goat anti-chicken Alexa Fluor 680; Supplementary
412 Table 4) antibodies diluted in blocking buffer. They were incubated at 37 °C for 4 days at each staining
413 step. The stained tissue was mounted in 1.5% w/v low melting point SeaPlaque™ agarose (#50101, Lonza,
414 Switzerland) and optically cleared using a BABB solution (benzyl alcohol (#1.09626.1000, Supelco, USA):
415 benzyl benzoate (#10654752, Thermo Fisher Scientific, USA) at 1:2).

OPT imaging was performed with an in-house developed near-infrared OPT system (described in detail in Eriksson et al. [69]), with a zoom factor of 1.6 or 2.0, that resulted in an isotropic voxel dimension of 16.5 μm^3 and 13.2 μm^3, respectively. To obtain specific fluorescent viral (NS5) signal (coupled with Alexa Fluor 680), and tissue autofluorescence signals, OPT images were acquired at the following filter settings: Ex: 665/45 nm, Em: 725/50 nm (exposure time: 7000 ms) and Ex: 425/60 nm, Em: 480 nm (exposure time: 500 ms), respectively.

To increase the signal-to-noise ratio for NS5, the pixel intensity range of all images was adjusted to display the minimum and maximum, and a contrast-limited adaptive histogram equalization (CLAHE) algorithm with a tile size of 64 × 64 was applied to projection images acquired in the NS5 channel [70]. Tomographic reconstruction was performed using NRecon software (v.1.7.0.4, Skyscan microCT, Bruker, Belgium) with additional misalignment compensation and ring artifact reduction. Image files were converted to Imaris files (.ims) using the Imaris file converter (v9.5.1, Bitplane, UK). NS5 signal from all imaged brains was adjusted to display at min = 0, max = 200, and gamma = 1.2, and colored using red glow color scheme. The signal was superimposed onto the corresponding tissue autofluorescence image using 3D iso-surface rendering in Imaris software (v9.5.1, Bitplane).

Light sheet fluorescent imaging

High-resolution images of ChP in the fourth ventricle of individual *Ifnar*$^{-/-}$ brains, previously scanned using OPT, were acquired by LSFM. To compensate for any phototoxic effects on immunofluorescence from homogeneous sample illumination during OPT acquisition, the sample was relabeled using both primary and secondary antibodies (see above) and cleared in BABB without agarose mounting. The brain was then scanned using an UltraMicroscope II (Miltenyi Biotec, Germany) with a 1× Olympus objective (PLAPO 2XC, Olympus, Japan), coupled to an Olympus zoom body providing 0.63–6.3× magnification with a lens-corrected dipping cap MVPLAPO 2×DC DBE objective (Olympus). For image acquisition, left and right light sheets were merged with a 0.14 numerical aperture, which resulted in a light sheet z-thickness of 3.87 µm

443 and 60% width, while using a 10–15 step blending dynamic focus across the field of view. Image sections
444 were generated by Imspector Pro software (v7.0124.0, LaVision Biotec Gmbh, Germany) and stitched
445 together using the TeraStitcher script (v9), implemented in Imspector Pro. Stitched images were then
446 converted into Imaris files (*.ims files) using the Imaris file converter (v9.5.1, Bitplane).
447
448 ***MRI acquisition***
449 After OPT, two brains were rehydrated in TBST. T1-weighted images were then acquired at 9.4 Tesla using
450 a preclinical MR system (Bruker BioSpec 94/20, Bruker, Germany) equipped with a cryogenic RF coil (MRI
451 CryoProbe, Bruker) running Paravision 7.0 software (Bruker). Specifically, Modified Driven Equilibrium
452 Fourier Transform (MDEFT) sequence with 5 repetitions (TR: 3000 ms; TE: 3 ms; TI: 950 ms; voxel
453 dimension: 40 × 40 × 40mm^3) was performed. Postprocessing of images involved the realignment and
454 averaging of individual repetitions using statistical parametric mapping (SPM8) (the Wellcome Trust Centre
455 for Neuroimaging, UCL, UK; www.fil.ion.ucl.ac.uk/spm) implemented in Matlab (R2014a, The MathWorks
456 Inc., USA).
457
458 ***Creation of OPT-MRI fusion images***
459 OPT images with viral signal and autofluorescence signal were reconstructed in DICOM format using
460 NRecon software (v.1.7.0.4, Bruker) followed by their conversion into NifTi using PMOD VIEW tool (v.4.2,
461 PMOD Technologies Inc., Switzerland) or the dcm2nii tool in MRIcron software for OPT and MR images,
462 respectively. Coregistration of OPT with the OCUM MRI template[21] was performed using the toolbox
463 SPMmouse in SPM8. Voxel-to-voxel affine transformation matrices were calculated using individual tissue
464 autofluorescence from OPT images and applied to the corresponding viral OPT images. Fusion images of
465 viral OPT signal were created for each individual brain using its own MRI and with the OCUM template
466 using the PMOD VIEW tool or Amira-Avizo software (v6.3.0, Thermo Fisher Scientific) for 3D renderings.
467 Finally, brain areas with viral signal were identified according to the Turone Mouse Brain Template and
468 Atlas (TMBTA) [45].
469

IHC for brain slices

Following euthanasia, cardiac perfusion with 4% PFA and PBS was performed as described above followed by immersion in 4% PFA at 4 °C overnight. PFA-fixed brain was washed in PBS, dehydrated overnight in a 30% w/v sucrose solution, snap-frozen on dry ice in Optimal Cutting Temperature medium (#361603E, VWR, USA), and stored at –80 °C until cryosectioning. The brain was sectioned along the sagittal plane at 10 µm thickness using a rotatory microtome cryostat (Microm Microtome Cryostat HM 500M, Microm, USA). Brain sections were permeabilized and blocked in 10% v/v NGS, 0.2% v/v TritonX-100, and 1% w/v bovine serum albumin in PBS for 1 h at room temperature (RT), immunolabelled with primary and secondary antibodies (Supplementary Table 4) diluted in 2% v/v NGS and 0.5% v/v TritonX-100 in PBS for overnight at 4 °C and 1 h at RT in the dark, respectively. Confocal fluorescence microscopy was performed using a Zeiss 710 confocal microscope (Zeiss, Germany) controlled by Zeiss Zen interface (v.14.0.19.201) with Axio Observer inverted microscope equipped with Plan Apochromat 20×0.8, C-Apochromat 40×/1.2, and Plan Apochromat 63×/1.4 objective lens or a Leica SP8 Laser Scanning Confocal Microscope equipped with HC PL APO 20x/0.75 (Leica), HC PL APO 40x/1.3 or HC PL APO 63x/1.40 and Leica Application Suit X software (LAS X, v.3.5.5, Leica). For quantification of microglial infection, a Leica SP8 Laser Scanning Confocal Microscope equipped with HC PL APO 20x/0.75 (Leica) and Leica Application Suit X software (LAS X, v.3.5.5, Leica) was used.

Quantification of microglial infection

Six slices (3 *Ifnar*$^{-/-}$ and 3 WT mice, 2 sections per animal) were co-stained for NS5 and Iba1 and the infected microglia were quantified in Imaris (v. 9.7.2). Therefore, stitched confocal images of the cerebrum were converted to .ims files using the Imaris file converter (v. 9.8.0). After background subtraction, a colocalization channel, displaying only cells positive for both NS5 and Iba1, was built using the “coloc” tool. Then, the “cell” function was applied to the NS5 and the colocalization channel to calculate the percentage of infected microglia, using a cell background subtraction width of 5 µm. The percentage of infected microglia was calculated for all slices and expressed as mean ± standard deviation (SD). Statistical analysis was performed using an unpaired two-tailed t-test with Welch´s correction in GraphPad Prism v9.3.1 (GraphPad Software Inc., San Diego, CA, USA). The level of significance was set at $p<0.05$.

497

498 ***Fixation, resin embedding, and staining of tissue for electron microscopy***

499 ChP from the brain of LGTV-infected *Ifnar*$^{-/-}$ mice were prepared for electron microscopy by cardiac
500 perfusion with 20 mL of 0.1 M phosphate buffer, followed by 20 mL of 2.5% w/v glutaraldehyde and 4% w/v
501 PFA in 0.1 M phosphate fixative solution. Fourth ventricle ChP was dissected and further immersed in the
502 same fixative solution for an additional 24 hours. The tissue was stained and subsequently embedded in
503 resin using the rOTO (reduced osmium tetroxide, thiocarbohydrazide, osmium tetroxide) method [71]. The
504 tissue samples were placed in a solution of 1.5% w/v potassium ferrocyanide and 2% w/v osmium tetroxide
505 (OsO4), and then incubated in Pelco Biowave Pro+ (Pelco, Fresno, USA), a microwave tissue processor
506 ("the processor"), under vacuum for 14 min. After two rinses with MilliQ water on the bench, the samples
507 were washed twice with MilliQ water in the processor without vacuum pressurization. Then, the samples
508 were incubated in 1% w/v thiocarbohydrazide solution for 20 min. After another MilliQ water rinse on the
509 bench, the samples were again washed twice in the processor (no vacuum). Next, the samples were placed
510 in 2% w/v OsO_4 solution and run in the processor under vacuum for 14 min, followed by an additional water
511 and processor wash. The samples were placed in 1% w/v uranyl acetate solution and run in the processor
512 under vacuum for 12 min, followed by another water and processor wash. The samples were then
513 dehydrated in a stepwise ethanol gradient series:30%, 50%, 70%, 80%, 90%, 95%, and 100%, twice in the
514 processor without vacuum. The dehydrated samples were infiltrated with an increasing concentration of
515 Durcupan ACM resin (Sigma-Aldrich) using the following stepwise ratios of ethanol to Durcupan resin: 1:3,
516 1:1, and 3:1 in the processor for 3 min under vacuum. The two final infiltration steps were performed in
517 100% resin. Finally, the samples were transferred to tissue molds, and placed at 60 °C for 48 h for complete
518 polymerization of the resin.

519

520 ***TEM***

521 Using a Reichert UltraCut S ultramicrotome (Leica, Germany), resin-embedded samples were trimmed,
522 and 50 nm sections were cut using a diamond knife and placed onto copper slot grids. Resin-embedded
523 sections were imaged using a 120 kV Talos L120C transmission electron microscope (Thermo Fischer

Scientific) fitted with a LaB6 filament and Ceta 4k × 4k CMOS camera sensor. Images were acquired at 2600×, 8500×, and 36,000× magnification corresponding to a pixel size of 54.3, 17.0, and 4.1 Å/px, respectively, at the specimen level. TEM images were analyzed by ImageJ software (NIH).

Volume imaging using FIB-SEM

Resin-embedded tissue blocks were trimmed, mounted on SEM stubs, and then coated with a 5 nm platinum layer using a Q150T-ES sputter coater (Quorum Technologies, UK) before FIB-SEM volume imaging. Data was acquired using Scios Dual beam microscope (FIB-SEM) (Thermo Fischer Scientific). Electron beam imaging was acquired at 2 kV, 0.1 nA current, 1.9 × 1.9 nm pixel spacing, 7 mm working distance, 10 µs acquisition time, and 3072 × 2048 resolution using a T1 detector. SEM images were acquired every 20 nm. The working voltage of gallium ion beam was set at 30 kV, and 0.5 nA current was used for FIB milling. The specimens were imaged at 5 × 5 µm block face and 5 µm depth. FIB milling and SEM imaging were automated using the Auto Slice and View software (Thermo Fischer Scientific). SEM volume images were aligned and reconstructed using ImageJ (NIH) with linear stack alignment, with SIFT and MultiStackRegistration plugins [72,73]. Analysis and segmentation of SEM volume images was done using Amira-Avizo software (v2020.3.1, Thermo Fisher Scientific).

Single nuclei isolation and sequencing

After euthanasia (day 5 for WT and day 3 for *Ifnar*$^{-/-}$), brains were collected in cold Hibernate A GlutaMAX medium (Thermo Fisher) without cardiac perfusion. Single nuclei were isolated from the cerebral cortex using the protocol modified from Gaublomme et al 2019 [74]. Cerebral cortexes from the hemisphere that did not receive needle injection from one male and one female mouse were manually dissected and homogenized in lysis buffer (10 mM Tris pH 7.4, 146 mM NaCl, 1 mM CaCl2, 21 mM MaCl2, 0.1% NP40 and 40 U/ml RNase inhibitor) using Dounce homogenizer for 10-20 times. Brain homogenates were washed with wash buffer (10mM Tris pH 7.4, 146 mM NaCl, 1mM CaCl2, 21 mM MaCl2, 0.01% BSA and 40 U/ml RNase inhibitor) and filter through 20 µm pre-separation filters (Miltenyi Biotec, 130-041-407) and were centrifuged with a swing bucket at 500xg, 4°C for 5 min. The supernatant was removed and resuspended

in the stain buffer (10 mM Tris pH 7.4, 146 mM NaCl, 1 mM $CaCl_2$, 21 mM $MaCl_2$, 2% BSA and 40 U/ml RNase inhibitor). Nuclei were stained with 10 µg/ml DAPI and subjected to sorting from cell debris using FACS (BD FACSAria III). The gate was set to sort for DAPI positive population (FSC 302, SSC 313 and BV421 313(log). The flow rate was adjusted to maintain about 10 nl/nuclei and with 80% efficiency. Sorted nuclei were transferred into low binding tubes and centrifuged using a swing bucket at 500xg, 4°C for 5 min. The overall quality of sorted nuclei was assessed under a microscope. Overall, 80% viable nuclei were then diluted for snRNAseq processing, using 10x Genomics 3' v2 kit according to manufacturer's instructions. The target recovery cells for WT and *Ifnar*$^{-/-}$ conditions were 8,800 cells. Reverse transcription, cDNA amplification and library construction were performed, and libraries were sequenced on an Illumina 6000 platform according to the manufacturer's instruction.

Data processing and quality control snRNA-seq

Demultiplexed reads were processed using CellRanger v6.1.2 with options expect-cells = 8000. All data sets were filtered prior to further processing. First, genes detected in fewer than 3 cells or nuclei with < 300 features were removed. A threshold of < 10% mitochondrial reads were applied and reads for the lncRNA Malat1 were removed. Potential doublets were addressed by i) removing cells with high number (> 5000) of detected features, ii) removing nuclei with co-expression of female and male genes (*Xist* and *Eif2s3y*) and iii) following cell annotation and subclustering of large cell types, removing distinct clusters showing co-expression of multiple cell type specific markers (e.g. neuronal and glial markers).

Cell annotation

Data analysis was performed in R version 4.2.1 using the Seurat package version 4.1.0 [75]. Data were normalized (NormalizeData), top 2000 variable features identified for each data set (FindVariableFeatures) and data integrated using FindIntegrationAnchors and IntegrateData in Seurat. The integrated expression matrix was scaled (ScaleData), subjected to principal component analysis (RunPCR) and the first 30 dimensions used as input for RunUMAP and to construct a shared nearest neighbor graph (SNN, FindNeighbors). Clustering was performed using FindClusters at resolution 1. Following data integration

and dimensional reduction/clustering, gene expression data (assay "RNA") was scaled and centered (ScaleData). The positive differential expression of each other cluster compared to all others (FindAllMarkers, test "wilcox") in combination with expression of established marker genes [76,77], Allen Brain Atlas, https://portal.brain-map.org/) was used to assign preliminary identities (excitatory neurons; neuron.ex, inhibatotry neurons; neuron.in, microglia/macrophages; micro/MØ, astrocytes; astro, oligodendrocytes; oligo, oligodendrocyte progenitor cells; OPC, vascular leptomeningeal cells; VLMCs, pericytes; peri, endothelial cells; endo, CD8+ T-cells and NK cells; CD8+NK, choroid plexus epithelial cells; ChP). Low-quality cells were identified as clusters with a combination of i) few significant differentially expressed genes and ii) high fraction of transcripts from mitochondrial and ribosomal genes and removed manually. To distinguish between microglia and other infiltrating immune cell population, this population was subsetted and the steps for dimension reduction, clustering and differential gene expression repeated.

DEG analysis and GSEA

Differentially expressed genes were identified using FindMarkers in Seurat, test MAST, applying a threshold of $\log_2$ fold change ($\log_2$FC) >1 and adjusted p values (padj) <0.05. GSEA was performed using the fgsea package version 1.22.0 in R [78]. Genes were ordered by average $\log_2$FC on the the MSigDB Reactome pathways obtained using the misgdbr package version 7.5.1. Pathways with a Benjamini-Hochberg corrected p-value <0.05 were considered significant. A comparison of mock (PBS) treated samples with untreated samples showed little transcriptional response to the injection procedure as such. Therefore, all further DEG analysis and GSEA was made comparing infected animals with uninfected (mock and untreated).

Isolation and infection of primary cells

Microglia were isolated from the astrocyte cultures as previously described [79] and grown in DMEM, supplemented with 10 % FBS, 100 U/mL of penicillin and 100 µg/mL streptomycin (Gibco), and mixed glial-conditioned medium (1:1). Monolayers of microglia were infected with LGTV (MOI 1) for 1 h at 37˚C and 5% CO_2 before the inoculum was removed and replaced with fresh medium. Cell supernatant was

harvested at 72 h post infection and viral titers determined by focus forming assay as previously described [26], and normalized to input control 3 hours post infection.

RNA extraction and RT-qPCR

Total RNA was extracted from cerebral cortexes from one hemisphere of infected mice were and viral replication quantified by qPCR as previously described [9]. In short, the cerebral cortex was manually dissected and homogenized in QIAzol Lysis Reagent (Quiagen) using 1.3 mm Chrome-Steel Beads (BioSpec) and the tissue homogenizer FastPrep-24 (MP). The RNA was extracted using the Nucleo-Spin RNA II kit (Macherey-Nagel). 1,000 ng of total RNA was used as input for cDNA synthesis using High-capacity cDNA Reverse Transcription kit (Thermo Fisher). LGTV RNA was quantified using qPCRBIO probe mix Hi-ROX (PCR Biosystems) and primers recognizing NS3 [15]. GAPDH was used as housekeeping gene, detected by QuantiTect primer assay (QT01658692, Qiagen) and the qPCRBIO SyGreen mix Hi-ROX (PCR Biosystems). All experiments were run on a StepOnePlus real-time PCR system (Applied Biosystems).

Acknowledgments

We thank G. Dobler (Bundeswehr Institute of Microbiology, Munich, Germany) for providing a stock of LGTV strain TP21; A. Pletnev (Laboratory of Infectious Diseases, NIAID, NIH, Bethesda, MD, USA) for providing the GFP-expressing LGTV infectious clone; and N.O. Gekara (Department of Molecular Biosciences, Stockholm University, Stockholm, Sweden) for providing the *Ifnar*$^{-/-}$ mouse colony. We thank M. Eriksson and C. Nord (UCMM, Umeå University, Umeå, Sweden) for OPT training, and J. Gilthorpe (Department of Integrative Medical Biology, Umeå University, Umeå, Sweden) for invaluable discussions. We also acknowledge Umeå Center for Microbial Research (UCMR); the Biochemical Imaging Center at Umeå University (BICU), and the National Microscopy Infrastructure for microscopy support; the Umeå Centre for Electron Microscopy (UCEM), a SciLifeLab National Cryo-EM facility for EM support; and the Small Animal Research and Imaging Facility (SARIF) at Umeå University, for MRI support. Single Cell Core Facility @ Flemingsberg campus (SICOF), Karolinska Institute, for their technical advice is gratefully acknowledged.

Illustration (Fig. 1a, 2b and 4a) were made with BioRender.com

Funding

NC and ES were supported by the MIMS Excellence by Choice Postdoctoral Program under the patronage of Emmanuelle Charpentier from the Kempe Foundation and Knut and Alice Wallenberg Foundation, grant SMK-1532 and KAW2015.0284, respectively. LAC was supported by the Swedish Research Council grant 2018-05851 and Wallenberg Centre for Molecular Medicine Umeå. DM was supported by Umeå University Medical Faculty, and AKÖ was supported by the Swedish Research Council grants 2020-06224 and 2018-05851, and the Laboratory for Molecular Infection Medicine Sweden (MIMS). JH is supported by the Swedish Research Council (Vetenskapsrådet) - grant number #2021-06602. ISM is supported by the Umeå University Industrial Doctoral School.

Data collection with confocal microscopy and EM were also supported by the Biochemical Imaging Center at Umeå University (BICU), and the National Microscopy Infrastructure (NMI; VR-RFI 2019-00217) and the Umeå Centre for Electron Microscopy (UCEM), a SciLifeLab National Cryo-EM facility and part of NMI (VR-RFI 2016-00968) grants from the Knut and Alice Wallenberg Foundation and Kempe Foundation, respectively. The computations were performed using resources provided by the Swedish National Infrastructure for Computing (SNIC) through the Uppsala Multidisciplinary Center for Advanced Computational Science (UPPMAX) under project SNIC 2022/5-18.

Author's contributions

NC, ER, SMAW, ES, JZ, LAC, UA, DM, AKÖ designed the experiment, NC, SMAW, ER and EN performed animal experiments, NC, SMAW, MH and EN acquired images and analyzed data from OPT, LSFM and confocal microscopy, SMAW, FM and DM acquired images and analyzed data from MRI and ES, JZ and LAC acquired images and analyzed data from EM. RL isolation, infection and analysis of microglia *in vitro*. NC, JH, IMS processed samples for snRNA sequencing, ER, JH and GE analyzed snRNA seq data. LAC,

UA, DM, JH and AKÖ supervised the experiments. NC, ER, SMAW, ES, LAC, UA, DM, AKÖ, wrote and edited the manuscript. All authors revised the manuscript.

Competing interests

Authors declare that they have no competing interests

Materials and Correspondence

All data generated or analyzed during this study are included in this published article and its supplementary information file. Raw image data can be requested from the corresponding authors with reasonable means to transfer large data files. Raw single nuclei RNAseq data is available at ArrayExpress #E-MTAB-12131. For the analysis, open-source algorithms were used as described in STAR Methods and all computer codes used for the analyses are available at https://github.com/ERosendal/LGTV_cortex_sn.

References

1 Sips, G. J., Wilschut, J. & Smit, J. M. Neuroinvasive flavivirus infections. *Rev Med Virol* **22**, 69-87, doi:10.1002/rmv.712 (2012).

2 Gosztonyi, G. & Koprowski, H. The concept of neurotropism and selective vulnerability ("pathoclisis") in virus infections of the nervous system--a historical overview. *Curr Top Microbiol Immunol* **253**, 1-13, doi:10.1007/978-3-662-10356-2_1 (2001).

3 Sejvar, J. J. The long-term outcomes of human West Nile virus infection. *Clin Infect Dis* **44**, 1617-1624, doi:10.1086/518281 (2007).

4 Turtle, L., Griffiths, M. J. & Solomon, T. Encephalitis caused by flaviviruses. *QJM* **105**, 219-223, doi:10.1093/qjmed/hcs013 (2012).

5 Gould, E. A. & Solomon, T. Pathogenic flaviviruses. *Lancet* **371**, 500-509, doi:10.1016/S0140-6736(08)60238-X (2008).

6 Ruzek, D. *et al.* Tick-borne encephalitis in Europe and Russia: Review of pathogenesis, clinical features, therapy, and vaccines. *Antiviral Res* **164**, 23-51, doi:10.1016/j.antiviral.2019.01.014 (2019).

7 Kubinski, M. *et al.* Tick-Borne Encephalitis Virus: A Quest for Better Vaccines against a Virus on the Rise. *Vaccines (Basel)* **8**, doi:10.3390/vaccines8030451 (2020).

8 Muller, U. *et al.* Functional role of type I and type II interferons in antiviral defense. *Science* **264**, 1918-1921, doi:10.1126/science.8009221 (1994).

9 Weber, E. *et al.* Type I interferon protects mice from fatal neurotropic infection with Langat virus by systemic and local antiviral responses. *J Virol* **88**, 12202-12212, doi:10.1128/JVI.01215-14 (2014).

10 Lazear, H. M., Pinto, A. K., Vogt, M. R., Gale, M., Jr. & Diamond, M. S. Beta interferon controls West Nile virus infection and pathogenesis in mice. *J Virol* **85**, 7186-7194, doi:10.1128/JVI.00396-11 (2011).

11 Samuel, M. A. & Diamond, M. S. Alpha/beta interferon protects against lethal West Nile virus infection by restricting cellular tropism and enhancing neuronal survival. *J Virol* **79**, 13350-13361, doi:10.1128/JVI.79.21.13350-13361.2005 (2005).

12 Lindqvist, R. *et al.* Fast type I interferon response protects astrocytes from flavivirus infection and virus-induced cytopathic effects. *J Neuroinflammation* **13**, 277, doi:10.1186/s12974-016-0748-7 (2016).

13 Fares, M. *et al.* Pathological modeling of TBEV infection reveals differential innate immune responses in human neurons and astrocytes that correlate with their susceptibility to infection. *J Neuroinflammation* **17**, 76, doi:10.1186/s12974-020-01756-x (2020).

14 Lindqvist, R., Kurhade, C., Gilthorpe, J. D. & Overby, A. K. Cell-type- and region-specific restriction of neurotropic flavivirus infection by viperin. *J Neuroinflammation* **15**, 80, doi:10.1186/s12974-018-1119-3 (2018).

15 Kurhade, C. *et al.* Type I Interferon response in olfactory bulb, the site of tick-borne flavivirus accumulation, is primarily regulated by IPS-1. *J Neuroinflammation* **13**, 22, doi:10.1186/s12974-016-0487-9 (2016).

16 Dionne, K. R., Galvin, J. M., Schittone, S. A., Clarke, P. & Tyler, K. L. Type I interferon signaling limits reoviral tropism within the brain and prevents lethal systemic infection. *J Neurovirol* **17**, 314-326, doi:10.1007/s13365-011-0038-1 (2011).

17 Zhao, L., Rose, K. M., Elliott, R., Van Rooijen, N. & Weiss, S. R. Cell-type-specific type I interferon antagonism influences organ tropism of murine coronavirus. *J Virol* **85**, 10058-10068, doi:10.1128/JVI.05075-11 (2011).

18 Sharpe, J. *et al.* Optical projection tomography as a tool for 3D microscopy and gene expression studies. *Science* **296**, 541-545, doi:10.1126/science.1068206 (2002).

19 Maffioli, C., Grandgirard, D., Engler, O. & Leib, S. L. A tick-borne encephalitis model in infant rats infected with langat virus. *J Neuropathol Exp Neurol* **73**, 1107-1115, doi:10.1097/NEN.0000000000000131 (2014).

20 Wang, Q. *et al.* The Allen Mouse Brain Common Coordinate Framework: A 3D Reference Atlas. *Cell* **181**, 936-953 e920, doi:10.1016/j.cell.2020.04.007 (2020).

21 Willekens, S.M. *et al.* An MR-based brain template and atlas for optical projection tomography and light sheet fluorescence microscopy. *bioRxiv* Pages 2022.11.14.516420, DOI: 10.1101/2022.11.14.516420 (2022).

22 Kim, J. *et al.* Zika virus infects pericytes in the choroid plexus and enters the central nervous system through the blood-cerebrospinal fluid barrier. *PLoS Pathog* **16**, e1008204, doi:10.1371/journal.ppat.1008204 (2020).

23 Welsch, S. *et al.* Composition and three-dimensional architecture of the dengue virus replication and assembly sites. *Cell Host Microbe* **5**, 365-375, doi:10.1016/j.chom.2009.03.007 (2009).

24 Miorin, L. *et al.* Three-dimensional architecture of tick-borne encephalitis virus replication sites and trafficking of the replicated RNA. *J Virol* **87**, 6469-6481, doi:10.1128/JVI.03456-12 (2013).

25 Mackenzie, J. M. & Westaway, E. G. Assembly and maturation of the flavivirus Kunjin virus appear to occur in the rough endoplasmic reticulum and along the secretory pathway, respectively. *J Virol* **75**, 10787-10799, doi:10.1128/JVI.75.22.10787-10799.2001 (2001).

26 Overby, A. K., Popov, V. L., Niedrig, M. & Weber, F. Tick-borne encephalitis virus delays interferon induction and hides its double-stranded RNA in intracellular membrane vesicles. *J Virol* **84**, 8470-8483, doi:10.1128/JVI.00176-10 (2010).

27 Herbert, J. *et al.* Transthyretin: a choroid plexus-specific transport protein in human brain. The 1986 S. Weir Mitchell award. *Neurology* **36**, 900-911, doi:10.1212/wnl.36.7.900 (1986).

28 Zhang, M. *et al.* Anti-West Nile virus activity of in vitro expanded human primary natural killer cells. *BMC Immunol* **11**, 3, doi:10.1186/1471-2172-11-3 (2010).

29 Patterson, C. E., Lawrence, D. M., Echols, L. A. & Rall, G. F. Immune-mediated protection from measles virus-induced central nervous system disease is noncytolytic and gamma interferon dependent. *J Virol* **76**, 4497-4506, doi:10.1128/jvi.76.9.4497-4506.2002 (2002).

30 Burdeinick-Kerr, R., Govindarajan, D. & Griffin, D. E. Noncytolytic clearance of sindbis virus infection from neurons by gamma interferon is dependent on Jak/STAT signaling. *J Virol* **83**, 3429-3435, doi:10.1128/JVI.02381-08 (2009).

31 Kang, S., Brown, H. M. & Hwang, S. Direct Antiviral Mechanisms of Interferon-Gamma. *Immune Netw* **18**, e33, doi:10.4110/in.2018.18.e33 (2018).

32 Cebrian, C., Loike, J. D. & Sulzer, D. Neuronal MHC-I expression and its implications in synaptic function, axonal regeneration and Parkinson's and other brain diseases. *Front Neuroanat* **8**, 114, doi:10.3389/fnana.2014.00114 (2014).

33 Zhou, F. Molecular mechanisms of IFN-gamma to up-regulate MHC class I antigen processing and presentation. *Int Rev Immunol* **28**, 239-260, doi:10.1080/08830180902978120 (2009).

34 Ochiai, E. *et al.* CXCL9 is important for recruiting immune T cells into the brain and inducing an accumulation of the T cells to the areas of tachyzoite proliferation to prevent reactivation of chronic cerebral infection with Toxoplasma gondii. *Am J Pathol* **185**, 314-324, doi:10.1016/j.ajpath.2014.10.003 (2015).

35 Trapani, J. A. Granzymes: a family of lymphocyte granule serine proteases. *Genome Biol* **2**, REVIEWS3014, doi:10.1186/gb-2001-2-12-reviews3014 (2001).

36 Zhang, Y. *et al.* A spatial and cellular distribution of rabies virus infection in the mouse brain revealed by fMOST and single-cell RNA sequencing. *Clin Transl Med* **12**, e700, doi:10.1002/ctm2.700 (2022).

37 Satoh, J. *et al.* TMEM119 marks a subset of microglia in the human brain. *Neuropathology* **36**, 39-49, doi:10.1111/neup.12235 (2016).

38 Alanentalo, T. *et al.* Tomographic molecular imaging and 3D quantification within adult mouse organs. *Nat Methods* **4**, 31-33, doi:10.1038/nmeth985 (2007).

39 Hahn, M. *et al.* 3D imaging of human organs with micrometer resolution - applied to the endocrine pancreas. *Commun Biol* **4**, 1063, doi:10.1038/s42003-021-02589-x (2021).

40 Dodt, H. U. *et al.* Ultramicroscopy: three-dimensional visualization of neuronal networks in the whole mouse brain. *Nat Methods* **4**, 331-336, doi:10.1038/nmeth1036 (2007).

41 Bocan, T. M., Panchal, R. G. & Bavari, S. Applications of in vivo imaging in the evaluation of the pathophysiology of viral and bacterial infections and in development of countermeasures to BSL3/4 pathogens. *Mol Imaging Biol* **17**, 4-17, doi:10.1007/s11307-014-0759-7 (2015).

42 Sunkin, S. M. *et al.* Allen Brain Atlas: an integrated spatio-temporal portal for exploring the central nervous system. *Nucleic Acids Res* **41**, D996-D1008, doi:10.1093/nar/gks1042 (2013).

43 Hikishima, K. *et al.* In vivo microscopic voxel-based morphometry with a brain template to characterize strain-specific structures in the mouse brain. *Sci Rep* **7**, 85, doi:10.1038/s41598-017-00148-1 (2017).

44 Dorr, A. E., Lerch, J. P., Spring, S., Kabani, N. & Henkelman, R. M. High resolution three-dimensional brain atlas using an average magnetic resonance image of 40 adult C57Bl/6J mice. *Neuroimage* **42**, 60-69, doi:10.1016/j.neuroimage.2008.03.037 (2008).

45 Barriere, D. A. *et al.* Brain orchestration of pregnancy and maternal behavior in mice: A longitudinal morphometric study. *Neuroimage* **230**, 117776, doi:10.1016/j.neuroimage.2021.117776 (2021).

46 Wilcox, D. R., Folmsbee, S. S., Muller, W. J. & Longnecker, R. The Type I Interferon Response Determines Differences in Choroid Plexus Susceptibility between Newborns and Adults in Herpes Simplex Virus Encephalitis. *mBio* **7**, e00437-00416, doi:10.1128/mBio.00437-16 (2016).

47 Stadtbaumer, K., Leschnik, M. W. & Nell, B. Tick-borne encephalitis virus as a possible cause of optic neuritis in a dog. *Vet Ophthalmol* **7**, 271-277, doi:10.1111/j.1463-5224.2004.04030.x (2004).

48 Fu, T. L., Ong, K. C., Tan, S. H. & Wong, K. T. Japanese Encephalitis Virus Infects the Thalamus Early Followed by Sensory-Associated Cortex and Other Parts of the Central and Peripheral Nervous Systems. *J Neuropathol Exp Neurol* **78**, 1160-1170, doi:10.1093/jnen/nlz103 (2019).

49 Vodicka, J., Jelinkova, H. & Chrobok, V. Smell impairment after tick-borne encephalitis vaccination: case report. *Vaccine* **28**, 886-888, doi:10.1016/j.vaccine.2009.11.012 (2010).

50 Figueiredo, C. P. *et al.* Zika virus replicates in adult human brain tissue and impairs synapses and memory in mice. *Nat Commun* **10**, 3890, doi:10.1038/s41467-019-11866-7 (2019).

51 Vasek, M. J. *et al.* A complement-microglial axis drives synapse loss during virus-induced memory impairment. *Nature* **534**, 538-543, doi:10.1038/nature18283 (2016).

52 Chauhan, P. S., Khanna, V. K., Kalita, J. & Misra, U. K. Japanese Encephalitis Virus Infection Results in Transient Dysfunction of Memory Learning and Cholinesterase Inhibition. *Mol Neurobiol* **54**, 4705-4715, doi:10.1007/s12035-016-9963-6 (2017).

53 Cornelius, A. D. A. *et al.* Langat virus infection affects hippocampal neuron morphology and function in mice without disease signs. *J Neuroinflammation* **17**, 278, doi:10.1186/s12974-020-01951-w (2020).

54 Pichler, A. *et al.* Magnetic resonance imaging and clinical findings in adults with tick-borne encephalitis. *J Neurol Sci* **375**, 266-269, doi:10.1016/j.jns.2017.02.003 (2017).

55 Gelpi, E. *et al.* Visualization of Central European tick-borne encephalitis infection in fatal human cases. *J Neuropathol Exp Neurol* **64**, 506-512, doi:10.1093/jnen/64.6.506 (2005).

56 Mishra, A. R., Byrareddy, S. N. & Nayak, D. IFN-I Independent Antiviral Immune Response to Vesicular Stomatitis Virus Challenge in Mouse Brain. *Vaccines (Basel)* **8**, doi:10.3390/vaccines8020326 (2020).

57 Raaben, M., Groot Koerkamp, M. J., Rottier, P. J. & de Haan, C. A. Type I interferon receptor-independent and -dependent host transcriptional responses to mouse hepatitis coronavirus infection in vivo. *BMC Genomics* **10**, 350, doi:10.1186/1471-2164-10-350 (2009).

58 Huang, K. W. & Sabatini, B. L. Single-Cell Analysis of Neuroinflammatory Responses Following Intracranial Injection of G-Deleted Rabies Viruses. *Front Cell Neurosci* **14**, 65, doi:10.3389/fncel.2020.00065 (2020).

59 Schneider, W. M., Chevillotte, M. D. & Rice, C. M. Interferon-stimulated genes: a complex web of host defenses. *Annu Rev Immunol* **32**, 513-545, doi:10.1146/annurev-immunol-032713-120231 (2014).

60 Hwang, M. & Bergmann, C. C. Neuronal Ablation of Alpha/Beta Interferon (IFN-alpha/beta) Signaling Exacerbates Central Nervous System Viral Dissemination and Impairs IFN-gamma Responsiveness in Microglia/Macrophages. *J Virol* **94**, doi:10.1128/JVI.00422-20 (2020).

61 Deczkowska, A., Baruch, K. & Schwartz, M. Type I/II Interferon Balance in the Regulation of Brain Physiology and Pathology. *Trends Immunol* **37**, 181-192, doi:10.1016/j.it.2016.01.006 (2016).

62 Ruzek, D. *et al.* CD8+ T-cells mediate immunopathology in tick-borne encephalitis. *Virology* **384**, 1-6, doi:10.1016/j.virol.2008.11.023 (2009).

63 Jain, N. *et al.* CD8 T cells protect adult naive mice from JEV-induced morbidity via lytic function. *PLoS Negl Trop Dis* **11**, e0005329, doi:10.1371/journal.pntd.0005329 (2017).

64 Shrestha, B. & Diamond, M. S. Role of CD8+ T cells in control of West Nile virus infection. *J Virol* **78**, 8312-8321, doi:10.1128/JVI.78.15.8312-8321.2004 (2004).

65 Wang, Y., Lobigs, M., Lee, E. & Mullbacher, A. CD8+ T cells mediate recovery and immunopathology in West Nile virus encephalitis. *J Virol* **77**, 13323-13334, doi:10.1128/jvi.77.24.13323-13334.2003 (2003).

66 Shrestha, B., Samuel, M. A. & Diamond, M. S. CD8+ T cells require perforin to clear West Nile virus from infected neurons. *J Virol* **80**, 119-129, doi:10.1128/JVI.80.1.119-129.2006 (2006).

67 Reinert, L. S. *et al.* Sensing of HSV-1 by the cGAS-STING pathway in microglia orchestrates antiviral defence in the CNS. *Nat Commun* **7**, 13348, doi:10.1038/ncomms13348 (2016).

68 Chhatbar, C. *et al.* Type I Interferon Receptor Signaling of Neurons and Astrocytes Regulates Microglia Activation during Viral Encephalitis. *Cell Rep* **25**, 118-129 e114, doi:10.1016/j.celrep.2018.09.003 (2018).

69 Eriksson, A. U. *et al.* Near infrared optical projection tomography for assessments of beta-cell mass distribution in diabetes research. *J Vis Exp*, e50238, doi:10.3791/50238 (2013).

70 Hornblad, A., Cheddad, A. & Ahlgren, U. An improved protocol for optical projection tomography imaging reveals lobular heterogeneities in pancreatic islet and beta-cell mass distribution. *Islets* **3**, 204-208, doi:10.4161/isl.3.4.16417 (2011).

71 Deerinck, T. J., Bushong, E. A., Thor, A. & Ellisman, M. H. *NCMIR methods for 3D EM: A new protocol for preparation of biological specimens for serial block face scanning electron microscopy* <https://www.ncmir.ucsd.edu/sbem-protocol> (2010).

72 Saalfeld, S. *Linear stack alignment with SIFT. https://imagej.net/imagej-wiki-static/Linear_Stack_Alignment_with_SIFT*, 2008).

73 Busse, B. & Miura, K. *MultiStackReg. https://biii.eu/multistackreg*, 2016).

74 Gaublomme, J. T. *et al.* Nuclei multiplexing with barcoded antibodies for single-nucleus genomics. *Nat Commun* **10**, 2907, doi:10.1038/s41467-019-10756-2 (2019).

75 Hao, Y. *et al.* Integrated analysis of multimodal single-cell data. *Cell* **184**, 3573-3587 e3529, doi:10.1016/j.cell.2021.04.048 (2021).

76 McKenzie, A. T. *et al.* Brain Cell Type Specific Gene Expression and Co-expression Network Architectures. *Sci Rep* **8**, 8868, doi:10.1038/s41598-018-27293-5 (2018).

77 Vanlandewijck, M. *et al.* A molecular atlas of cell types and zonation in the brain vasculature. *Nature* **554**, 475-480, doi:10.1038/nature25739 (2018).

78 Sergushichev, A. A. An algorithm for fast preranked gene set enrichment analysis using cumulative statistic calculation. *BioRxiv*, doi:https://doi.org/10.1101/060012 (2016).

79 Saura, J., Tusell, J. M. & Serratosa, J. High-yield isolation of murine microglia by mild trypsinization. *Glia* **44**, 183-189, doi:10.1002/glia.10274 (2003).

Figures

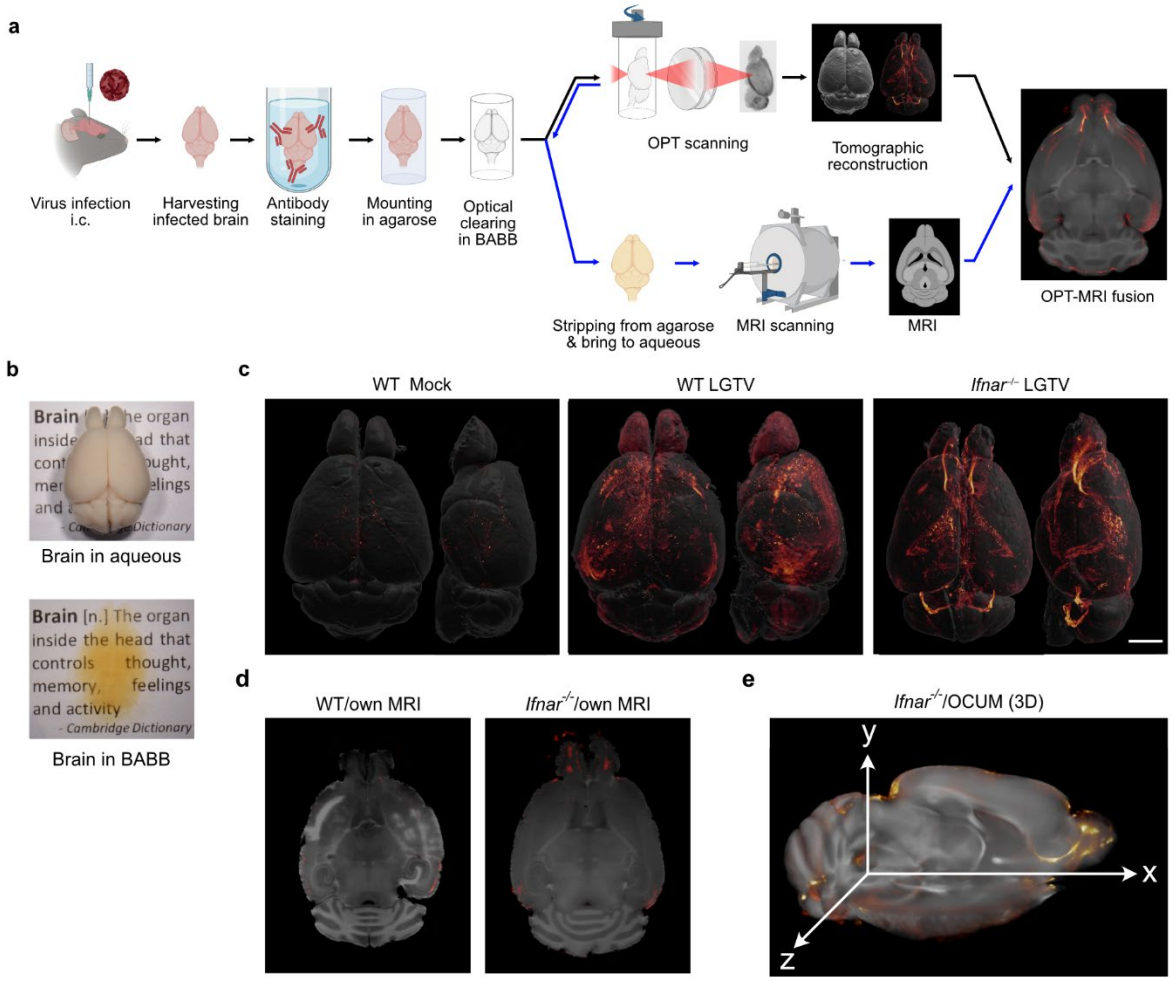

Fig 1. Whole brain 3D imaging of viral infection. a A workflow for viral infection and whole brain imaging. **b** Mouse brain appearance in aqueous and in optical clearing solvent, BABB. **c** Volumetric 3D-render of the brain of mock and LGTV infected brains immunolabeled with anti-NS5 antibody (virus marker; red glow). The signal intensity was normalized within an individual brain and adjusted to identical minimum and maximum. For each image pair, the top and lateral views of the same specimen are shown. Five mice per group were analyzed. Representative images are shown here, and the remaining brains (n = 4) are shown in Supplementary Fig. 1b. Scale bar = 2000 μm. **d** OPT-MRI fusion image created using viral OPT signal (red) with own MR scan of WT and *Ifnar*$^{-/-}$ brains. **e** 3D mapping of viral OPT signal with the OCUM template.

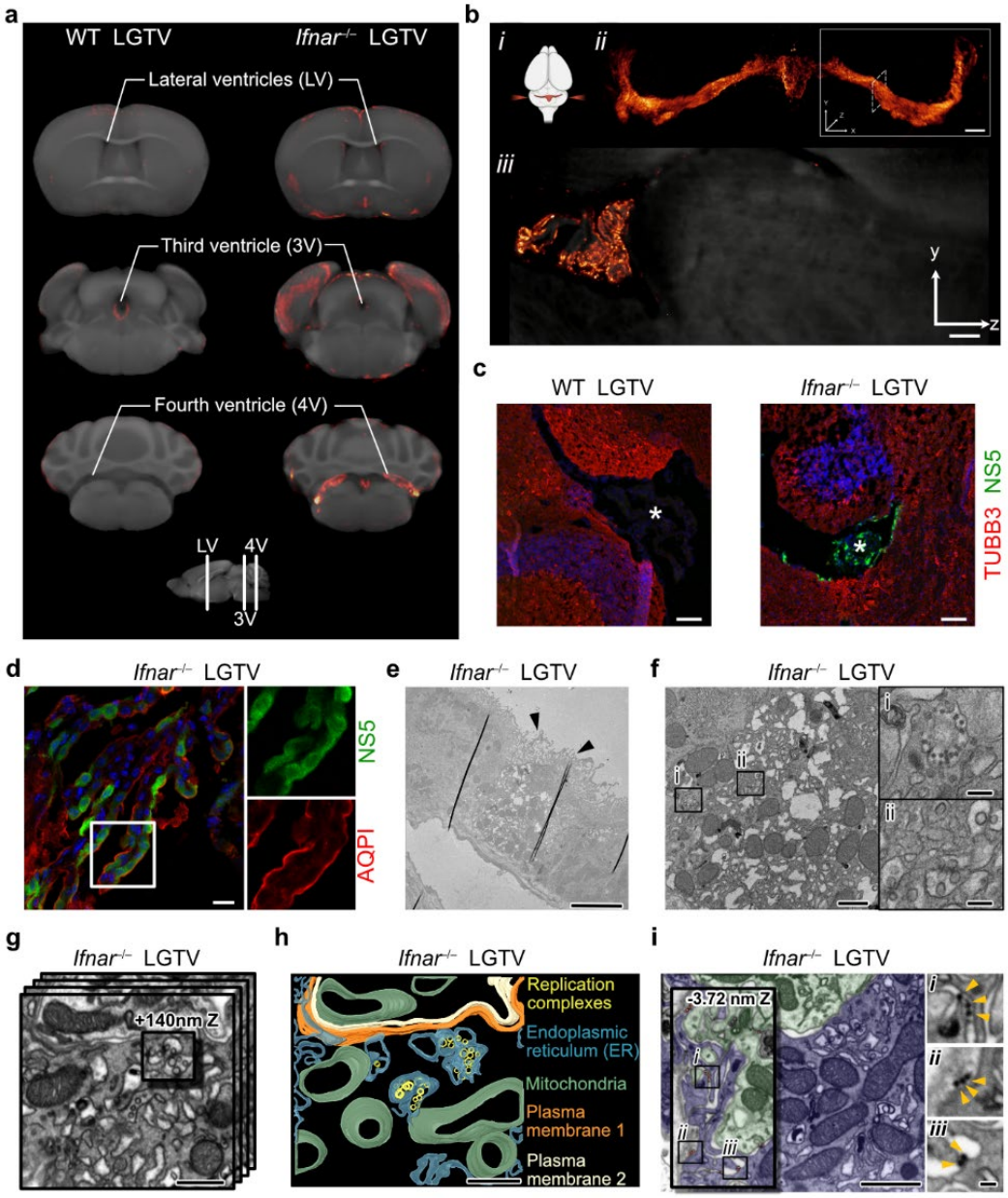

880

881 **Fig. 2. Viral infection in ChP showed the protection by IFN-I response. a** OPT-MRI mapping viral
882 infection from OPT signal (red) onto the OCUM template (gray), focusing at the lateral, third and fourth
883 ventricles. Images were shown in three representative coronal plains as indicated in the bottom panel.
884 **b** LSFM showing high-resolution image of the fourth ventricle ChP infected with LGTV. (*i*) Orientation of the
885 brain in the LSFM during image acquisition. (*ii*) Volumetric 3D render of LSFM of LGTV infected fourth
886 ventricle ChP, immunolabeled with anti-NS5 antibodies (red glow). ChP was imaged in 3 tiles at 2.5×

magnification and stitched together with 20% overlap. z = 2000 µm; scale bar = 300 µm. Solid-line square indicates the area imaged and dashed-line square shows the orientation of (*iii*). (*iii*) Tomographic section viewed from the YZ plane at 4× magnification. **c** Confocal images of infected cells in the fourth ventricle ChP.ChP (indicated by asterisk) of WT and *Ifnar*$^{-/-}$ brains, were immunolabeled with antibodies against NS5, mature neuron (TUBB3) and nucleus (DAPI; blue). Scale bars = 100 µm. **d** Maximum intensity projection of confocal z stack capturing fourth ventricle ChP, immunolabeled with antibodies against NS5 and ChP epithelial cell (AQPI) Scale bars = 20 µm. **e** Ultrastructure of virus replication complex in ChP of *Ifnar*$^{-/-}$ brain by electron microscopy. Low-magnification TEM image of ChP epithelial cells with a heavily infected cell indicated by dilated ER membrane. Black arrows indicate cilia on the apical side of ChP epithelial cells. Scale bar = 5 µm. **f** High-magnification TEM of ChP epithelial cell in (e). Scale bar = 1 µm. Insets show high magnification images of (*i*) virus particles and (*ii*) replication complexes within dilated ER. Scale bar = 200 nm. **g** FIB-SEM volume imaging shows viral replication complexes within dilated ER. Scale bar = 500 nm. **h** Segmentation image created from the 3D volume images in (g). Animation is shown in the Supplementary Movie 3. Scale bar = 500 nm. **i** FIB-SEM slice-through volume image of two infected cells (blue and green). Scale bar = 1 µm. Inset shows different z depths of the same volume. Boxes *i-iii* (left) show apparent released virus particles between the cilia, also displayed as enlarged images (right, arrowheads). Scale bar = 100 nm. The confocal images represent n=3/genotype; 2 slices/brain, and the EM images represent n=2 brains; 3-5 technical replicates.

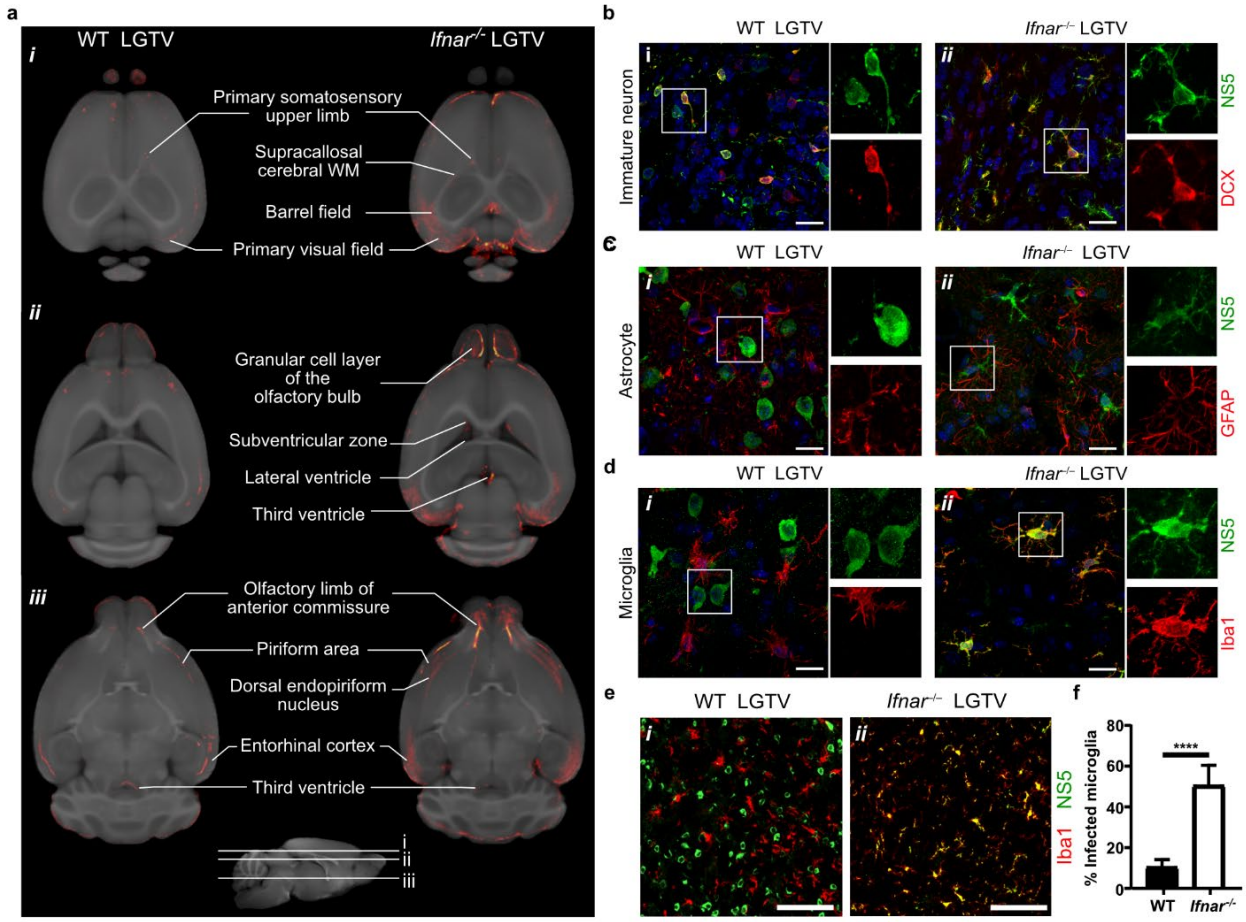

Fig. 3. Imaging of viral infection revealed cellular tropisms and tropism shift shaped by IFN-I response. a Anatomical mapping of brain regions after coregistration of viral OPT signal (red) with the OCUM brain template (gray). Images of WT and *Ifnar*$^{-/-}$ infected brains are shown in three representative axial plains as indicated in the bottom panel. **b-d** Maximum-intensity projection of confocal z-stack. The images were taken from sagittal brain sections (10 µm) using confocal microscope (n=3 per genotype). Scale bars = 20 µm. **b** Captured at the granule cell layer of olfactory bulb. The sections were immunolabeled using antibodies against viral NS5, doublecortin (DCX) for immature neurons in the rostral migratory stream and nucleus (DAPI; blue). **c** Ccaptured within entorhinal cortex and piriform area. The sections were immunolabeled with antibodies against viral NS5, GFAP for astrocyte and nucleus. **d** Captured within entorhinal cortex and piriform area. The sections were immunolabeled using antibodies against viral NS5, Iba1 for microglia, and nucleus (DAPI; blue). **e** Low magnification images show representative fields of the

sagittal slices of cerebral cortex stained with NS5 and Iba1 in WT and *Ifnar*$^{-/-}$ brains. Scale bars = 100 µm. **f** Percent of Iba1-positive infected cells of total number of infected cells in cortical slices. Statistical analysis showed a significant difference (****, $p < 0.0001$) between the percentage infected Iba1-positive cells in *Ifnar*$^{-/-}$ mice as compared to WT (n=3 per genotype and 2 slices per brain).

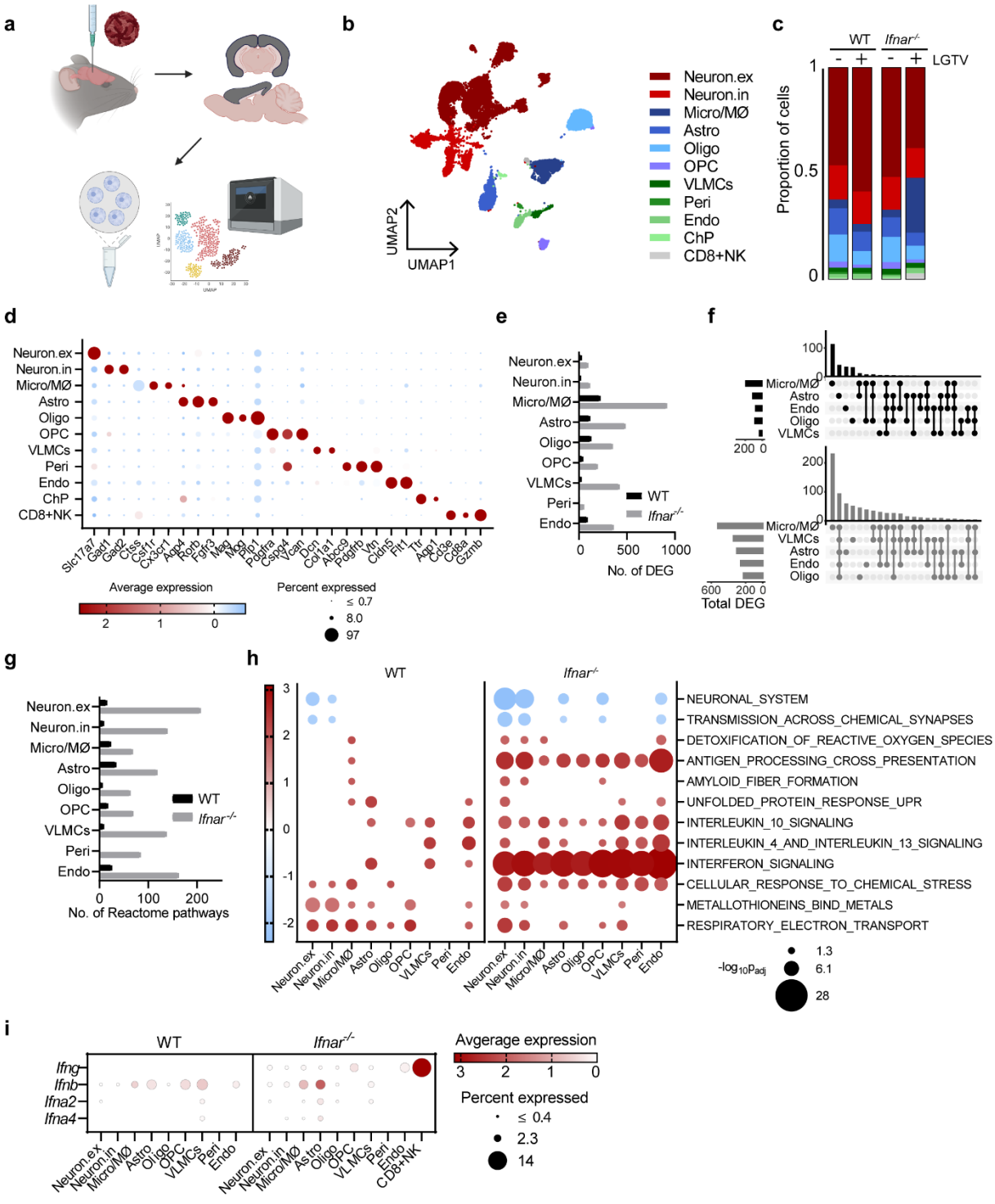

Fig. 4. Single nuclei RNA sequencing (snRNAseq) analysis of transcriptional response to LGTV infection. a Schematic overview of the workflow. **b** Uniform Manifold Approximation and Projection (UMAP) of 28,298 nuclei captured by droplet based snRNAseq (10x) colored by assigned identities;

925 excitatory neurons; neuron.ex, inhibitory neurons; neuron.in, microglia/macrophages; micro/MØ,
926 astrocytes; astro, oligodendrocytes; oligo, oligodendrocyte progenitor cells; OPC, vascular
927 leptomeningeal cells; VLMCs, pericytes; peri, endothelial cells; endo, natural killer and CD8+ T-cells;
928 NK/CD8, choroid plexus epithelial cells; ChP. **c** Relative proportion of each cell type in uninfected and
929 LGTV infected samples. **d** Dotplot showing expression of canonical marker genes used to identify major
930 cell types. **e** Number of DEGs ($log_2FC>1$, $p_{adj} < 0.05$) induced by LGTV infection in WT or *Ifnar*$^{-/-}$ mice. **f**
931 Overlap in upregulated DEGs between five most reactive cell types, shown as a modified UpSet plot for
932 WT and *Ifnar*$^{-/-}$ separately. **g** Number of significant REACTOME pathways following LGTV infection in
933 WT or *Ifnar*$^{-/-}$ mice. **h** DotPlot showing examples of Reactome pathways altered by infection, color
934 corresponding to Normalized Enrichment Score and size corresponding to $-log_{10}$ adjusted p-value. i
935 DotPlot showing expression of IFN-I and IFN-II upon infection of WT and *Ifnar*$^{-/-}$ mice.
936

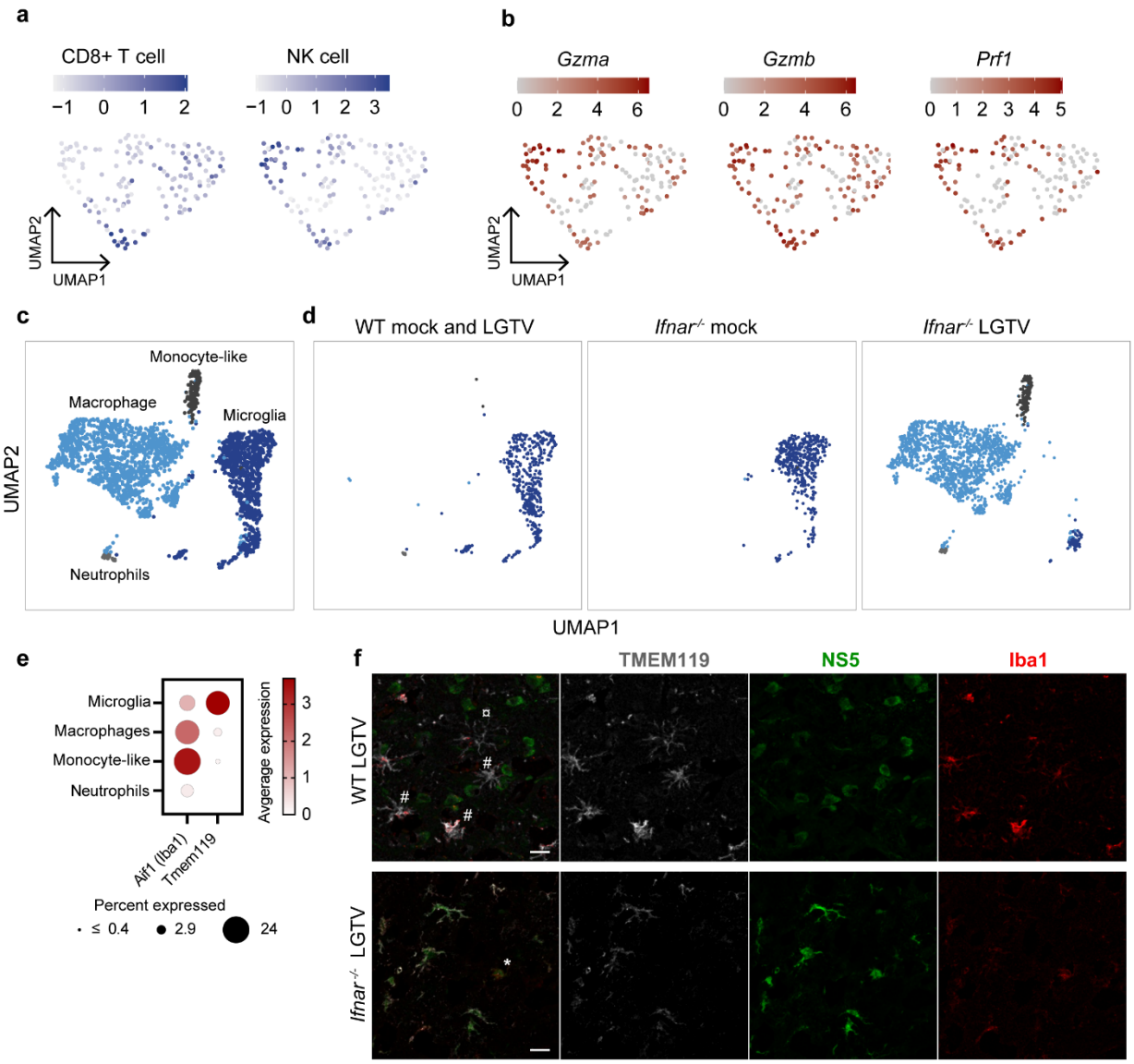

937

938 **Fig. 5. Infiltrating immune cells during LGTV infection in *Ifnar*$^{-/-}$ mice.**

939 **a** Subclustering of 147 nuclei of CD8+NK cell subset found in infected *Ifnar*$^{-/-}$, colored by gene signatures

940 for NK cells (*Klrblc, Klrd1, Nrc1, Nkg7*) or CD8+ T cells (*Cd3g, Cd3d, Cd28, Cd8a, Cd8b1*). **b** UMAP plot

941 colored by expression levels of granzyme A (*Gzma*), B (*Gzmb*) and perforin (*Prf1*) **c** Subclustering of

942 2,401 nuclei of micro/MØ cell subset belonging to all datasets, colored by assigned identities visualized

943 by UMAP; Microglia, Macrophages (MØ), Monocyte-like cells and Neutrophils. **d** UMAP from (c) showing

944 nuclei from WT mock and LGTV, *Ifnar*$^{-/-}$ mock and *Ifnar*$^{-/-}$ LGTV, respectively. **e** DotPlot showing

945 expression of *Aif1* (Iba1) and *Tmem119* in cell subtypes. **f** Maximum-intensity projection of confocal z-
946 stack captured within the sagittal slices of cortex. The sections were immunolabeled with antibodies
947 against viral NS5 (green), Iba1 (red) and TMEM119 (white) in WT and *Ifnar*$^{-/-}$ brains. ¤ resting state
948 microglia, # different activated sates of resident microglia and * infiltrating macrophage. Scale bar = 20
949 µm.

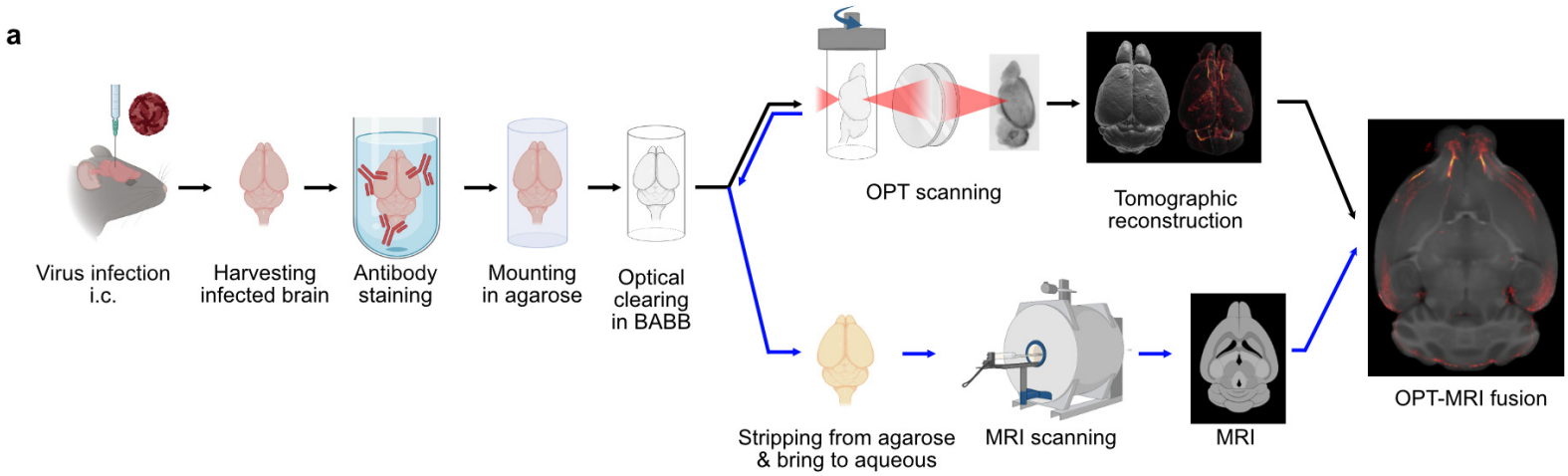

b

Brain in aqueous

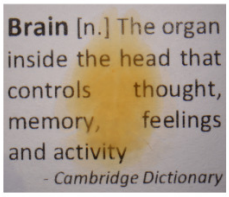

Brain in BABB